



**UNIVERSITY OF LEEDS**

**Simulating Iron and Silicon Atoms:  
Investigating Earth's  
Inner Core Nucleation Paradox**

Word Count: 9,949

Sulayman Birt

Student ID: 201342787

Supervisors: Prof. C. Davies & Dr. A. Wilson

Submitted in accordance with the requirements for the degree of  
Bachelor of Geophysical Sciences

The University of Leeds

Faculty of Environment

School of Earth and Environment

May 2022

The candidate confirms that the work submitted is his own and that appropriate credit has been given where reference has been made to the work of others.

This copy has been supplied on the understanding that it is copyright material and that no quotation from the thesis may be published without proper acknowledgement.

© 2022 The University of Leeds and Sulayman Birt

The right of Sulayman Birt to be identified as Author of this work has been asserted by him in accordance with the Copyright, Designs and Patents Act 1988.

## Acknowledgements

I would like to thank Chris Davies and Alfred Wilson for all the great help they gave me in completing this project. I very much enjoyed our weekly discussions and I appreciated your advice on how to solve the different challenges I faced with this project. Lots of love as well to my Mum, Dad, and Layla for all their help and support.

## Abstract

Recent studies have suggested that before the Earth's inner core can nucleate and grow, a substantial energy barrier to the formation of stable atomic clusters must be overcome. This is achieved through critical undercooling of  $\sim 700\text{--}1000\text{K}$  below the melting temperature of the iron alloy. However, the core cools at  $\sim 100\text{ K/Gyr}$ , but has existed for less than 1 billion years, and we have detected its presence seismically. Its observed existence cannot be reconciled with collected results, thereby leading to the inner core nucleation paradox.

Studies of core composition and densities predict an iron inner core alloyed with lighter elements like silicon, oxygen, and sulphur. A 2019 study has made use of atomic-scale molecular dynamics (MD) simulations to investigate the effects of iron–oxygen alloys on inner core nucleation. This current study is the first to investigate the incorporation of silicon and makes use of the same direct simulation (DM) simulation method to collect data on the waiting time to observe a freezing event in iron–silicon mixtures. Thermodynamic parameters are constrained to make a fit to the data, and we extrapolate a value for the critical undercooling to determine silicon alloying with iron reduces the nucleation barrier

We obtain a final critical undercooling value of  $69 \pm 69\text{ K}$ . However, this value is highly uncertain, and we have been unable to make a statistically sound fit to the poor-quality data. We cannot currently use our results to infer if iron–silicon lowers the nucleation barrier or compare to the results of previous studies. Further studies should use a mixture of DM and pre-freezing nuclei (PN) simulation methods, for pure iron, iron–oxygen, iron–sulphur, and iron–silicon systems, to work towards solving the nucleation paradox.

# Contents

Acknowledgements .....	ii
Abstract .....	iii
List of Figures .....	vi
List of Tables .....	vii
1. Introduction .....	1
1.1 – Earth's Magnetic Field and Core .....	1
1.2 – Age of the Inner Core .....	2
1.3 – Inner Core Nucleation and Growth .....	3
1.4 – The Nucleation Paradox .....	4
1.5 – Studies of the Paradox .....	6
1.6 – Analysing the Previous Methods .....	9
1.7 – The Nucleating Phase of Iron .....	11
1.8 – Modelling Initial Core Freezing .....	12
1.9 – The Core Composition .....	14
1.10 – Aims and Objectives .....	15
2. Methodology .....	16
2.1 – Classical Nucleation Theory .....	16
2.2 – Atomic Simulations .....	18
2.3 – Making Use of LAMMPS .....	19
2.4 – Equations of State .....	20
2.5 – Iron–Silicon Melting Temperature .....	22
3. Results .....	24
3.1 – Temperature and Pressure Data .....	24
3.2 – Average Waiting Times .....	25
3.3 – Atomic Structure .....	26
3.4 – Critical Undercooling Results .....	27
3.5 – Distributions of the Data .....	29
4. Analysis & Discussion .....	32
4.1 – Uncertainties .....	32
4.2 – Data Quality .....	32
4.3 – Thermodynamic Parameters .....	33

4.4 – Analysis of Methodology.....	34
4.5 – Investigating a Refit.....	35
4.6 – Investigating the Available Undercooling.....	37
4.7 – Homogeneous Solutions .....	39
4.8 – Heterogeneous Solutions .....	40
4.9 – Future Work.....	41
5. Conclusions.....	43
References.....	44
Appendices .....	49
Section A – Supplementary Plots .....	50
Section B – CNT Derivations.....	52
Section D – Details of LAMMPS Simulations .....	54
Section E – Equations of State and Thermal Expansion .....	56
Section F – Melting Temperature Uncertainty .....	59
Section G – Waiting Times to Freeze and Uncertainties .....	60
Section H – Earth Centre Undercooling .....	64

## List of Figures

Figure 1 – Literature Waiting Time for a Given Undercooling. ....	13
Figure 2 – Change in Gibb’s Free Energy against Radius of Nuclei. .....	17
Figure 3 – Birch–Murnaghan Equations of State.....	21
Figure 4 – Temperature and Pressure against Time.....	24
Figure 5 – Simulation Snapshots.....	27
Figure 6 – Measured Waiting Time for a Given Undercooling.....	28
Figure 7 – Histograms of Waiting Time Data .....	31
Figure 8 – Refitted Waiting Time for a Given Undercooling .....	36
Figure 9 – Undercooling at Earth’s Centre against Undercooled Layer Radius .....	38
Figure A1 – Equilibration of the System.....	50
Figure A2 – Radial Distribution Functions.....	51
Figure A3 – Atomic Density .....	52
Figure D2 – Example LAMMPS Script.....	56

## List of Tables

Table 1 – Studies of Homogeneous Nucleation.....	6
Table 2 – Thermodynamic Parameters.....	12
Table C1 – EAM Parameters.....	53
Table D1 – Boxes of Atoms Parameters.....	55
Table E1a – EOS Parameters .....	57
Table G1 – Waiting Time Data .....	62
Table G2 – Average Waiting Times .....	64
Table H1 – Available Undercooling Parameters .....	65



# 1. Introduction

## 1.1 – Earth's Magnetic Field and Core

The early geomagnetic field sheltered Earth's atmosphere from erosion and solar winds, which would have helped to enable the conditions under which water and life developed and continues to shield the Earth in the present day (Tarduno et al., 2010). The geomagnetic field is generated by dynamo action and turbulence in Earth's electrically conductive fluid outer core (Roberts & Glatzmaier, 2000). Kinetic energy converts to magnetic energy and is associated with vigorous thermal convection which is powered by heat-flow across the core–mantle boundary and Earth's surface that is lost to space. (Gubbins, 1977). This thermal and chemical convection is driven by Earth's cooling and the crystallization of its inner core, where gravitational energy arises through segregation of light elements in the alloy during freezing and the mixing of elements to restore a minimum gravitational potential energy.

The molten core formed during accretion but has undergone secular cooling, which has a secondary role in driving the geodynamo alongside latent heat (Nimmo et al., 2015). Crystallization releases latent heat that drives thermal buoyancy, and partitions light elements which causes compositional convection through chemical buoyancy, thereby powering the geomagnetic field (Labrosse & Macouin, 2002). This heat loss because of Earth's cooling is known as primordial heat, with there also being heat generation in the form of radiogenic heat, which produces geoneutrinos that are detected by large subsurface instruments (Dye, 2010). Palaeointensity determinations in ancient silicate crystals can be used to describe the evolution of convection in the mantle and show that the field has persisted the past 3.4–3.45 billion years

(Tarduno et al., 2014). The growth history of the Earth describes and depends on the evolution of the geodynamo.

## 1.2 – Age of the Inner Core

There is great variety in the different estimates for the age of the inner core. Theoretical and experimental studies have suggested that core thermal and electrical conductivities are 2–4 times higher than previously thought, which implies a high core heat flux down the adiabat of  $>8$  TW, a young inner core ( $< 1$  Ga) and rapid core cooling (Pozzo et al., 2012; Gomi et al., 2013; Gubbins et al., 2015). Models of thermal evolution with a well-mixed superadiabatic core and core-mantle boundary heat flow can produce low inner core ages of  $\sim 600$  Myr old or greater, and much higher early core temperatures. (Davies, 2015; Labrosse 2015). These similar results from different modelling routes arise because these models which incorporate a higher thermal conductivity predict there being less power available to the geodynamo, so a higher core cooling rate is needed to provide more power to maintain the same field, and much higher past temperatures are produced. Earth's growth history is recorded in the distribution and magnitude of deformation-texturing induced seismic anisotropy, with travel time observations being modelled and supporting a younger inner core ( $\sim 0.5 - 1.5$  Ga). Ultimately, placing constraints on models of core cooling helps to solve the nucleation paradox, which is the focus of this investigation and will be explained subsequently.

Palaeomagnetic evidence for the start of inner core nucleation is sparse and some datasets in the Precambrian database overestimate the field strength, with the spatial and temporal sampling of the field insufficient to make

robust conclusions, putting doubt on the recent constraints placed on thermal conductivity (Smirnov et al., 2016; Lasbleis et al., 2019). It was previously thought that the magnetic field was powered solely by thermal convection and secular core cooling before crystallization of the inner core (Labrosse & Macouin, 2002). However, it has recently been suggested that exsolution of magnesium-bearing mantle components could help drive compositional buoyancy in the early geodynamo prior to nucleation and somewhat explain the palaeomagnetic records predating inner core age estimates, due to the predicted increase in thermal conductivity. (O'Rourke & Stevenson, 2016; Badro et al., 2016; Hirose et al., 2017; Badro et al., 2018). Crystallization of SiO<sub>2</sub> over the core can allow for an older inner core of > 1 Ga, so the onset of inner core growth has significant implications in terms of Earth's thermal and magnetic histories.

### 1.3 – Inner Core Nucleation and Growth

Conventionally, it is thought that the inner core started growing from the bottom up and cooling by conduction after the temperature at its centre dropped below the melting point of its iron alloy where solid metal is thermodynamically stable, and that this steady growth was determined by the mantle thermal history (Labrosse et al., 1996). However, new studies have suggested a substantial nucleation energy barrier to the formation of stable nuclei must be surmounted through critical undercooling of Earth's core before nucleation of the core can begin, which previous models of core nucleation have not accounted for (Huguet et al., 2018, Davies et al., 2019).

For solidification to occur below the melting temperature of a liquid, a thermodynamic energy barrier must be overcome before a stable crystalline atom cluster can form, which is due to the solid–liquid interface energy exceeding the volumetric energy and there being a physical energy requirement to create a new surface (Christian, 2002). This difference between the two energies, which are labelled as volumetric and interfacial, and cooling below the liquidus temperature are what determine the nucleation energy barrier size, and therefore the growth of crystal nuclei. Critical undercooling is a requirement for a critical radius of growth to be reached and for equilibrium of the system, and not necessarily just core temperatures falling below the liquidus (Davies et al., 2019; Wilson et al., 2021).

This critical radius is the radius of nuclei beyond which there is crystallisation, and the probability of continued growth increases exponentially. Embryos at this point have an equal chance of growing or remelting and past this point there is solidification of the system. (Davies et al., 2019). Undercooled metal alloy liquids are thought to resist crystallization due to small–scale icosahedral symmetry following x-ray structural studies (Kelton et al., 2003). Homogeneous nucleation is nucleation that arises away from a surface whilst heterogeneous nucleation involves a surface or some form of solid seed that reduces the exposed surface area of a nucleus.

## 1.4 – The Nucleation Paradox

The nucleation paradox arises because the large undercooling, which was initially calculated theoretically as ~1000 K by Huguet et al. (2018), required for crystallization to begin, is too large when considering the ~100

K/Gyr secular cooling of the core since accretion and the young inner core age of ~1 billion years inferred from high thermal conductivity (Huguet et al., 2018). Despite the unexplained undercooling that was required to form the present inner core, we can observe its existence seismically. A maximum value of only around 200 K of undercooling can possibly be provided by secular cooling when comparing the radius of the inner core surface with the required undercooling to form it.

Following inner core nucleation, it is believed that a mush layer develops at the inner core boundary while the outer core fluid freezes (Shimizu et al., 2005). Late inner core crystallization, if delayed by undercooling, would see an initial fast growth phase of a spherical region around the innermost core below the liquidus temperature, after the nucleation barrier was passed, followed by quick transition to slow growth (Huguet et al., 2018; Lasbleis et al., 2019). The freezing of this large region under the melting temperature would result in a very large inner core that exceeds current observations. Liquid trapped near the inner core surface would vary greatly in quantity depending on this growth phase, allowing constraints to be placed on undercooling through seismic detection of crystal textural porosity variations and spikes in thermal and chemical buoyancy that would impact the geodynamo field.

Greater critical undercooling values mean greater delays in the onset of nucleation. Better understanding critical undercooling places improved constraints on age of the inner core and its thermal history, and therefore the power sources available to the geodynamo, which is what drives the processes behind observed palaeointensity variations.

## 1.5 – Studies of the Paradox

<u>Study</u>	<u>Modelled substance</u>	<u>Method</u>	<u>Calculated Critical Undercooling Value</u>
Huguet et al. (2018)	hcp iron	Thermodynamic estimate	> 1000 K
Davies et al. (2019)	hcp iron	DM simulation	730 ± 20 K
Davies et al. (2019)	hcp iron with oxygen	DM simulation	675 ± 35 K
Sun et al. (2021)	hcp iron	PEM simulation	610 K
Sun et al. (2021)	bcc iron	PEM simulation	470 K
Wilson et al. (2021)	hcp, bcc and fcc iron	PN simulation	807 K
This study	hcp iron with silicon	DM simulation	69 ± 69 K

*Table 1 – Different studies of homogeneous nucleation in the core without any external effects, and the modelled substance, method and calculated critical undercooling for each.*

Huguet et al.'s (2018) first determination of the critical undercooling of ~1000 K used experimental and simulated constraints of thermodynamic parameters, referred to as a thermodynamic estimate method. They calculate the critical undercooling by defining the waiting time to observe freezing events as

$$\tau_v = \frac{1}{2I_0} \exp \left[ \frac{16\pi\gamma^3 T_m^2}{3k_B T \Delta T_c^2 h_f^2 h_c^2} \right]. \quad (1)$$

where  $h_f$  is the enthalpy of fusion and  $h_c$  is a correction accounting for non-linearity of the free energy difference, for which Davies et al. use a value of  $1 - 7.046 \times 10^{-5} \Delta T$ , and  $k_B$  is the Boltzmann constant (Christian, 2002; Davies et al., 2019).  $\Delta T$  is the undercooling below  $T_m$ , the substance melting temperature, for a given temperature  $T$  ( $\Delta T = T - T_m$ ), leading to  $\Delta T_c$ , which is the critical undercooling value. The kinetic prefactor  $I_0$  relates to the amount of atoms in each unit volume and an attempt frequency of atoms forming embryos, with the typical given value of  $10^{42}$  not being not well constrained, and the free interfacial energy  $\gamma$  is the energy associated with the creation of a surface between solid and liquid material. Equation 1 is fully derived in Appendix B. This study was subsequently followed up by several others which are highlighted in Table 1.

Davies et al. (2019) have made a direct assessment of the paradox through estimating thermodynamic parameters and calculating the required undercooling following MD simulations of iron and iron alloys and the core conditions required for them to freeze. These simulations constrain the factors  $I_0$  and  $\gamma$  by treating them as free parameters and fitting to directly simulated data of the waiting time to observe freezing events at different undercooling values. The achieved critical undercooling values are  $730 \pm 20$  K for the pure iron simulations and  $675 \pm 35$  K for the iron–oxygen simulations, which are a lot lower than the previous estimate of 1000 K and highlights that light elements in the core, such as oxygen, can be a means of reducing the nucleation barrier, although these values still must be greatly reduced to solve the paradox.

Sun et al. have published a study recently looking at nucleation of the bcc phase of iron rather than the hcp phase, which has already been

determined to require a great degree of undercooling in Davies et al. (2019). They utilise a persistent embryo method (PEM) of measuring the critical nucleus size by detecting fluctuations around this critical value, and to obtain parameters such as the kinetic prefactor  $I_0$ , alongside a specially developed semi-empirical potential, within MD simulations of bcc iron particles at inner core conditions. It is suggested that metastable bcc nucleation is the first step of inner core crystallisation and growth rather than solely nucleation of the hcp phase, with critical undercooling values of 470 K for bcc phase iron and 610 K for hcp phase iron, making this a potential means of moving towards solving the paradox.

The work of Davies et al. (2019) has been followed up by a study that presents a new way of understanding the nucleation process in iron within the inner core by looking at systems at low to medium undercooling, where the waiting times are outside of the range that was accessible to Davies et al. (2019) (Wilson et al., 2021). This approach collects data on solid-like subcritical nuclei, in other words nuclei at radii below the critical value, specifically their distributions and similarity to solid bonding configurations around central atoms, inside undercooled iron liquid at inner core pressures. This is to predict critical nuclei and thermodynamic parameters that best describe subcritical nuclei are fit to waiting times.

This study finds a critical undercooling of 807 K corresponding to the waiting time to freeze for inner core conditions, and that defect-rich hcp characterizes the nucleating material in the inner core, in contrast to the results of Sun et al. (2021). However, one similarity is that both suggest that the observed frozen solid material is different to the theoretically most stable, bulk solid material, and that this lower free energy solid is what makes the system



freeze at a lower undercooling. The results of this study serve to support the required undercooling calculated by Davies et al. (2019) by utilising a new method to arrive at a similar value.

## 1.6 – Analysing the Previous Methods

The work of Huguet et al. (2018), is very important to this field of study as it was the first to propose the paradox, although very uncertain estimates were used for the prefactor  $I_0$  and solid–liquid free interfacial energy  $\gamma$  in calculation, which were adapted from previous different studies that were not necessarily relevant to nucleation at inner core conditions, and casts doubt on the required undercooling produced (Davies et al., 2019).

Subsequent DM simulations by Davies et al. (2019) used measured data to greatly constrain these parameters and therefore improve the undercooling estimate. However, the problem with this method is that due to limits in computational power, accessible waiting times are limited to values of  $10^{-31}$  s  $\text{m}^3$  which is over 60 orders of magnitude smaller than the waiting time estimated for the inner core of  $2.3 \times 10^{35}$  s  $\text{m}^3$  (Davies et al., 2019). Essentially, DM simulation methods assume that the behaviour of a box of atoms with a very small mass and volume over a period on the order of ns is representative of the greatly significantly larger inner core over its one–billion–year age. Davies et al. (2019) conclude that, although fitted thermodynamic parameters are quite different to previous values and other empirical relationships can be fitted to the data, this extrapolation of CNT shows a reasonable fit to the data. The primary way to remove this extrapolation is to utilise the PN method utilised in Wilson et al., 2021 and considering temperatures much closer to the melting point.

The method of this study along with Davies et al. (2019) assumes that the nucleating phase is hcp iron and liquid iron, whereas Wilson et al. (2021) do not make that assumption and consider nucleation of all phases and any thermodynamic properties, thereby not being biased towards behaviours following CNT, but, conversely, they assume that small nuclei energies represent those of critical nuclei. This is a big assumption to make, as these are groups of particles that do not contribute towards freezing of the iron alloy or, therefore, towards nucleation of the inner core and are groups of particles that are statistically very likely to refreeze, with only nuclei at sizes greater than the critical size having a high probability of growing indefinitely. In future, this assumption would need to be investigated and possibly verified by comparing the behaviours and thermodynamic properties of subcritical and critical nuclei. The DM simulation method requires the constraining of thermodynamic parameters by fitting the waiting time curve to data, which the need for is bypassed in Sun et al. (2021) through directly obtaining parameters through using the PEM, although they do fit the parameters for the pair potentials to data.

The main issue with the work of Sun et al. (2021) is that they are effectively imposing a bcc structure on the simulated particles, and it could be argued that bcc structure nuclei are observed because the code already presupposes their formation before inferring the critical nuclei values. A damping function is used to keep atoms solid that are under conditions such that they would melt and hold atoms around crystal sites. This means that the final derived undercooling values for bcc phase iron may not be representative of the nucleation behaviour of iron alloys at inner core conditions due to this initial bias. It is also argued that nonclassical nucleation would be necessary to

describe the two-step process rather than it being based in Classical Nucleation Theory (CNT), which is the theory utilised by Huguet et al. (2018) and Davies et al. (2019) to describe inner core nucleation (Wilson et al., 2021). This method could perhaps be improved by simulating iron particles and utilising code that looks for bcc particle structure in the system, and then these embryos could be the ones utilised in the PEM to infer the critical nuclei size, and therefore the required undercooling value, removing the bias in structure. However, this method does in fact utilise particle potentials specifically tailored to simulating iron at inner core conditions, which is an improvement over previous studies.

This issue is not present in the work of Wilson et al. (2021), whose method of using spherical harmonics to define bonding environments and pick out what is solid-like behaviour in observed atom arrangements does not presuppose any structure, and therefore has no structural bias in the derived undercooling value. In conclusion, these studies have achieved different results for the critical undercooling due to their very different methods and assumptions, but all provide important insights into the problem, so a mixture of methods may be ideal for further studies.

## 1.7 – The Nucleating Phase of Iron

It is debated whether body-centred cubic (bcc) or hexagonal close-packed (hcp) is the stable crystalline phase of iron at the high temperature and pressure conditions of the inner core, which influences the substance melting temperature (Belonoshko et al., 2003; Côté et al., 2008; Asanuma et al., 2008; Fischer et al., 2013). There are also contentions in which of these phases is stabilised by the incorporation of silicon (Tsuchiya et al., 2009, Tateno et al.,

2015, Belonoshko et al., 2017). The work of Sun et al. (2021) finds that the hcp phase is thermodynamically stable whilst the bcc phase is metastable between the core–mantle boundary and inner core boundary. The work of Wilson et al. (2021) has no bias in the nucleating phase and finds that defect rich hcp phase best characterizes inner core nucleation. However, despite there being significantly more studies that support a hcp structure of iron, changes in phase do not directly affect our simulation process, so for our study we use parameters that prefer the hcp structure.

## 1.8 – Modelling Initial Core Freezing

<u>Study</u>	<u>Modelled substance</u>	<u><math>I_0</math> Value</u>	<u><math>\gamma</math> Value</u>
Huguet et al. (2018)	hcp iron	$10^{-40}$	1.2
Davies et al. (2019)	hcp iron	$0.71 \pm 2.9 \times 10^{-48}$	$1.08 \pm 0.02$
Davies et al. (2019)	hcp iron with oxygen	$0.79 \pm 4.0 \times 10^{-45}$	$1.02 \pm 0.04$
Wilson et al. (2021)	hcp, bcc and fcc iron	$\sim 10^{-42}$	1.02
Modelled Secular Cooling	hcp iron	$0.71 \times 10^{-48}$	0.59
This Study	hcp iron with silicon	$1.76 \pm 0.30 \times 10^{-35}$	$0.22 \pm 0.22$

*Table 2 – Thermodynamic parameters which are used to fit Equation 1 to waiting time data in this study and in Davies et al. (2019). Parameters are given for the key studies as well as for this study and for the modelled secular cooling which is shown in Figure 1 below.*

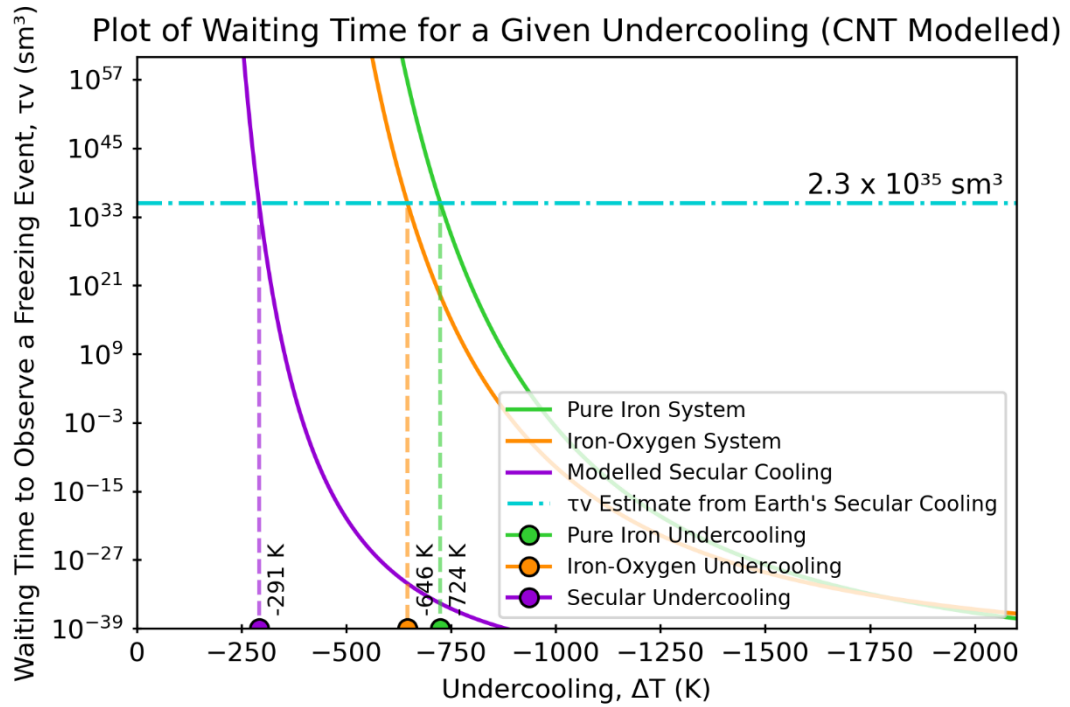


Figure 1 – Waiting time for a given undercooling, using the thermodynamic parameters constrained by Davies et al. (2019) to model Equation 1 based on their pure iron and iron–oxygen simulations. These quantities are the waiting time to observe freezing events and the undercooling below the substance melting temperature. Solid green and orange lines model the undercooling required based on the given parameters for those systems, which are shown in Table 2. Dashed blue line indicates waiting time required for 1 freezing event to occur in the volume occupied by the current inner core, which is  $2.3 \times 10^{35} \text{ sm}^3$ . Dashed green and orange lines extrapolate the undercooling for inner cores composed of pure iron and iron–oxygen respectively. Solid and dashed purple lines show the shift in waiting times that would be required to reduce the undercooling to the improbable maximum value possible with Earth’s secular cooling (<291 K), with the parameters shown in Table 2.

Figure 1 highlights the large shift in waiting times that would be required to reduce the undercooling to <291 K. This is a value we have calculated ourselves (see Appendix H and Figure 9), as a very improbable maximum value for comparison with the literature calculated inner core undercooling values in Table 1. The lowest critical undercooling value any study has produced for homogeneous nucleation is 470 K, which is still much too high, even when

using a very unlikely high estimate for the available undercooling (Sun et al., 2021).

Davies et al. (2019) have looked at the effects of alloying of iron with oxygen on inner core nucleation since several studies of core composition have some amount of oxygen, averaging around ~3 wt% (Hirose et al., 2013). Oxygen also does not enter the solid at core conditions so is the primary cause of the observed density difference between the solid and liquid, along with the depression in the core melting temperature,  $\chi_0$ . For the modelled secular cooling in Figure 1, we only adjust the parameter  $\gamma$  and keep  $I_0$  the same as for pure iron in Davies et al. (2019), to highlight the great change in one parameter required to bring the required undercooling to more reasonable values. The values of required undercooling derived using the parameters of Davies et al. (2019) vary slightly differently from the values they have given, which can be seen in Table 1, but as they are within error, this is not an issue.

## 1.9 – The Core Composition

The composition of the core has been estimated using the ratios between major and trace elements and comparing meteorite correlation diagrams to balance the mantle depletion of silicon and gives a value of 7.3 wt% silicon in the core (Allegre et al., 1995). Studies of Si–isotope fractionation in enstatite meteorites and terrestrial rocks to represent Earth’s differentiation of silicon into metal during core formation give a value of ~6 wt% core silicon (Shahar et al., 2009, Ziegler et al., 2010). These values of 6–8 wt% silicon matching the density deficit of the liquid core compared to pure iron are supported by an Equation of State (EOS) up to 407 GPa and 5960 K (Tateno et

al., 2015). Energy dispersion spectra from reactions between liquid iron and  $\text{SiO}_3$  perovskite demonstrate that Si dissolution into molten iron is greatly increased at higher pressures (Takafuji et al., 2005). High-pressure x-ray scattering experiments producing sound velocities give varying inner core values of 2.3 wt% up to 5 wt% silicon more recently. (Badro et al., 2007, Edmund et al., 2019). At least 3 wt% Si is expected to be present in the inner core where there is chemical equilibrium (Tsuchiya et al., 2009). These studies all show that the core is highly likely to contain some amount of silicon, which is why we consider in this study its effects on inner core nucleation, and, importantly, this is the first known investigation into this alloy.

In terms of matching outer core densities and compositions, the 2.7 wt% composition we use is within the range of reasonable values. If this low-end composition lowers the undercooling, the results of this study could possibly describe the minimum undercooling provided by silicon alloying, which could be higher with increased silicon content. A value that is too low would not change the system from pure iron enough that we could possibly see any differences, so we use a high enough value that may lead to a change. Ideally, we would use a composition that is from when the inner core started to freeze, although this would be very difficult to source as even present-day estimates of composition are not well constrained.

## 1.10 – Aims and Objectives

This study aims to complete the following:

- Use a DM simulation method and collect data on the waiting time to freeze iron–silicon mixtures

- Constrain CNT thermodynamic parameters to make a statistically sound fit to the data
- Extrapolate a value for the critical undercooling, and therefore determine if silicon alloying with iron will reduce the nucleation barrier
- Determine if further MD simulation studies of differing natures and methodologies could be used to try solving the paradox, by considering silicon as one of many required steps

## 2. Methodology

### 2.1 – Classical Nucleation Theory

CNT approximates the nucleation of substances and was developed following the works of Gibbs (Christian, 2002). The interplay between internal free energy, which scales volumetrically, and solid–liquid interfacial energy, which scales with surface area, determines the stability of crystal nuclei (Turnbull, 1950). Gibb’s free energy is a thermodynamic potential which represents the maximum reversible work that a system can undergo at a certain temperature or pressure.

The change in Gibb’s free energy can be thought of as the amount of free energy available to do work and is defined as

$$\Delta G = \frac{4}{3}\pi r^3 g_{SL} + 4\pi r^2 \gamma, \quad (2)$$

where  $r$  is the nucleus radius,  $g_{SL}$  is the difference between solid and liquid internal free energies ( $g_{SL} = g_S - g_L$ ). At thermodynamic equilibrium, where there are no net flows of matter or energy, a system is found in the state of



minimum Gibb's free energy difference, where pressures and temperatures are spatially uniform.

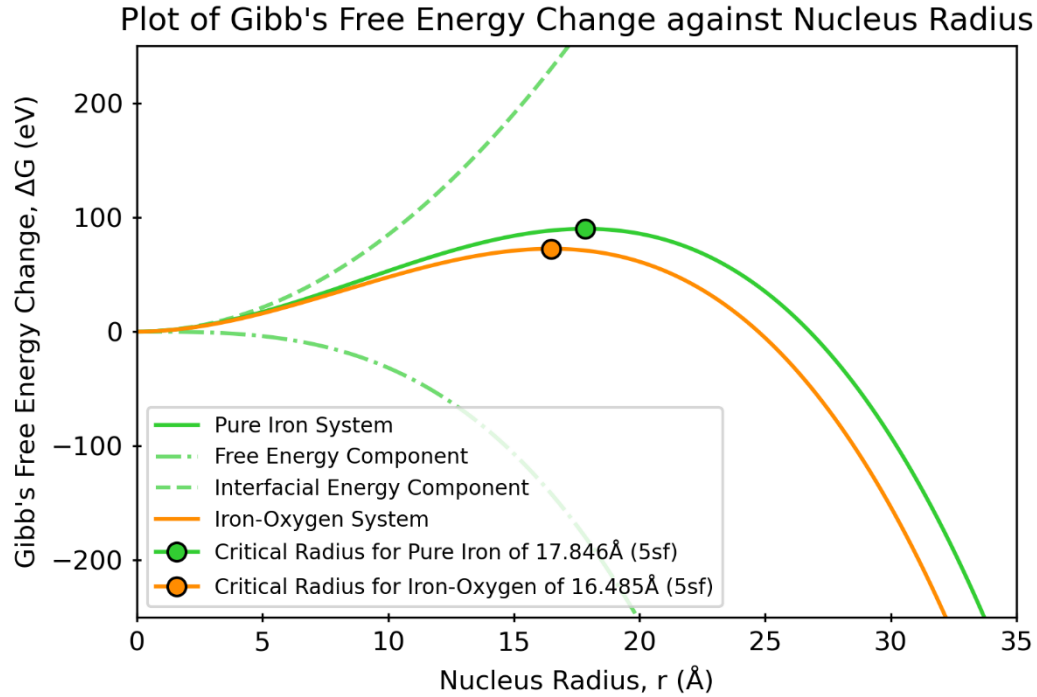


Figure 2 – Change in Gibb's Free Energy against radius of nuclei for pure iron and iron–oxygen systems using thermodynamic parameters constrained in Davies et al. (2019) by simulations in Equation 2. Solid green and orange lines show the Gibb's free energy change for pure iron and iron–oxygen respectively, with the critical radius for each highlighted. Gibb's free energy change for pure iron is separated into the interfacial energy component (dashed green line) and free energy component (dot-dashed green line).

Figure 2 gives a visual representation of the top of the nucleation barrier and the critical radius. Initially, the negative free energy term has a smaller magnitude than the positive interfacial energy term, so the Gibb's free energy change increases with undercooling until the point at which they have equal magnitude, which is the critical radius point at the top of curve. Past this, the magnitude of the negative interfacial energy becomes increasingly greater, so the Gibb's free energy change quickly decreases. The nucleation rate remains

negligible until close approach of the critical undercooling, increases quickly for greater undercooling but then reduces abruptly at very low temperatures (Huguet et al., 2018).

## 2.2 – Atomic Simulations

This study will simulate iron–oxygen mixtures at the inner core pressure of 323 GPa and at different undercooling values until the system freezes, allowing for direct measurement of waiting time to freeze, assuming that freezing events are stochastic processes with a distribution of waiting times, as in Davies et al. (2019). At each temperature, 50 simulations will be run and used to calculate an average waiting time, with each simulation having the same kinetic energy but statistically independent random velocities.

This study will utilise an embedded atom model, which is a semiempirical model designed for simple and transition metals, to quantitatively define the potentials between iron and silicon atoms (Daw & Baskes, 1983; Daw, 1989). The total internal energy is modelled with a pair interaction function and a repulsive pair potential which describe a force depending on the separation of two atoms (Sutton & Chen, 1990). Each atom, embedded in a lattice with all others, is used to always define the electron density and therefore the energy of the metal. Density Functional Theory is a computational modelling method that defines the electronic structure of a particle system by replicating behaviours and properties of different materials and can be used to calculate free energies and chemical potentials in solid–liquid mixtures (Alfè et al., 2002b).

Set parameters (Appendix Table C1) are used in equations (Appendix C1–6) to define potential curves modelling the behaviour of the different atom combinations at different distances. The Fe parameters come from a study of metal melting properties, where these parameters have been fit to their *ab initio* energies of the solid and liquid states (Alfè et al, 2002b). A potential for silicon has yet to be published, so the Si and Fe–Si parameters have been found by members of the research team by following the method used to obtain the EAM parameters in Davies et al. (2019). The parameters have been fit using *ab initio* methods based in DFT by fitting the EAM equations to recorded energies and pressures (See Appendix C).

## 2.3 – Making Use of LAMMPS

The EAM is utilised within LAMMPS simulations, which is a MD simulation program in which boxes of atoms are set up using various potentials and parameters to model different states of matter. These MD simulations are used to model iron–silicon as, despite DFT calculations being much more complex and detailed, they are limited to short timescales and small systems due to the much higher computational intensity, and to integrate Newtonian equations of motion to calculate particle trajectories (Allen, 2004). MD approximates atoms as classical particles and uses this to calculate atomic forces and system energy by allowing atoms and molecules to interact for a set amount of time.

The EAM potentials calculated are predefined in DFT rather than being calculated in real time, and then using these to calculate forces between the particles, reducing simulation times by eliminating one step of the calculations.

MD simulations are used to approximate these iron–silicon mixtures due to the long timescales and large system size required when modelling undercooled liquid metals in the inner core. The exact process by which the simulations are conducted can be seen in Appendix D. A simulation length of 1 ns is used as this value is long enough such that sufficient time is given for most simulations to freeze, but short enough such that simulation times do not become too long, for more of them to be conducted. The systems we are using are equilibrated and there is no apparent drift (see Appendix Figure A1).

The LAMMPS code used to run these simulations was adapted from previous MD work, but many iterations were required to have the correct box properties and ensure that the particles were behaving in the correct way. It took several months and many trial simulations to fix problems with particle behaviour and to optimize the code so that simulations could be automated and run simultaneously and in quick succession. The Python code required to create the figures in this work was also created from scratch, and a lot of time was required to automate the creation of plots and outputting of useful information from each simulation. Each of the 150 simulations we have collected took around 3–4 hours to complete after being submitted as jobs to the Arc4 Supercomputer. Several hundred jobs were required in total when accounting for the initial setup of the simulations, and for each job, three nodes were utilised, each with 40 pins.

## 2.4 – Equations of State

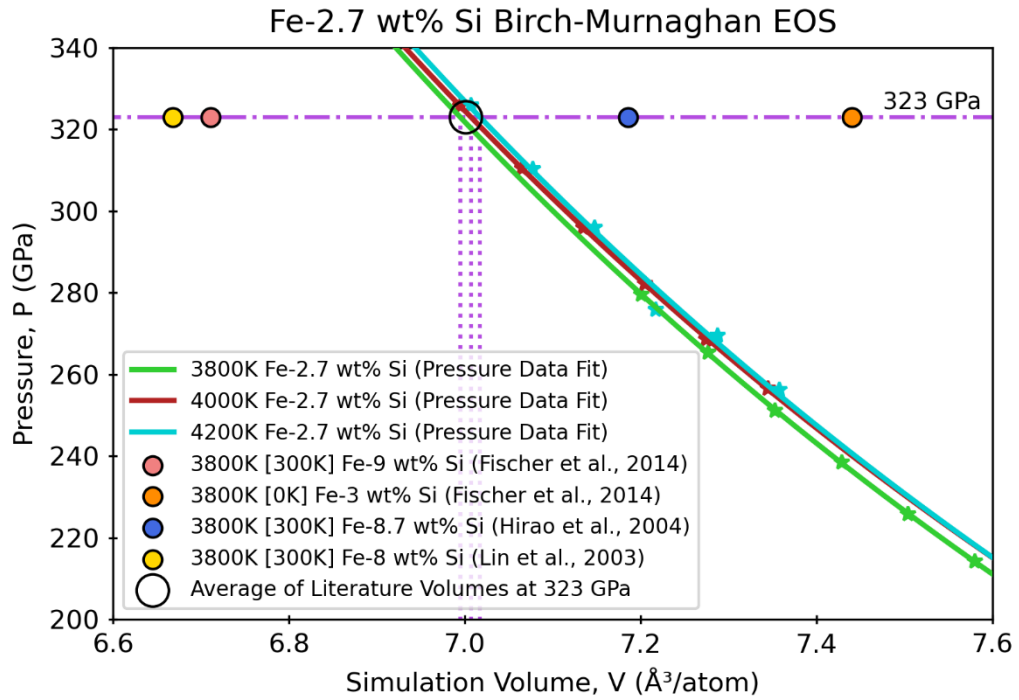


Figure 3 – Birch-Murnaghan equations of state showing estimated pressures for a given simulation volume. Green, red, and blue points are measured data whilst solid green, red and blue lines are Birch Murnaghan Fits to the data by evaluating Appendix Equation E1 with parameters that can be seen in Appendix Table E1a. Horizontal dashed purple line is at the goal pressure of 323 GPa, and the ideal volume values of the EOS functions at 323 GPa are shown with the vertical dashed purple lines. The pink, orange, blue and yellow circles represent literature Birch-Murnaghan equations of state for different Iron–silicon alloys that have been extrapolated to 3800K using thermal expansivity, with parameters available in Appendix Table E1b. These circles show the ideal volume values of each literature EOS at 323 GPa. The transparent circle is the average of these ideal volumes for all four literature values.

For our simulations, a pressure of 323 GPa is utilised as this is the pressure of the inner core boundary, where crystallisation of liquid takes place, such that a direct comparison can be made to Davies et al. (2019) who use the same value for their studied systems. This pressure is set by using a certain volume at the temperature of interest, with these ideal volumes being estimated using a Birch–Murnaghan EOS shown in Appendix Equation E1 below, which is plotted in Figure 3 and determined by the fitted parameters in Table E1a. The

pressure data used in the equations of state comes from an average system pressure over the last 1000 timesteps of the system equilibration phase, prior to when the main simulation starts, and the temperatures are allowed to vary.

The expanded literature equations of state seen in Figure 3 are only approximations and are likely to be inaccurate due to the significant temperature difference between the original temperatures and there being a big temperature extrapolation up to 3800K. We assume that the value of  $\alpha$  increases linearly when it follows much more complex behaviour. Furthermore, most of these studies have much higher silicon contents, so therefore can only give a loose indication of the validity of our fitted EOS curves, and there appears to be a reasonable spread between their volumes at 323 GPa. However, taking the average value of these extrapolated 3800K ideal volumes gives a value of 7.001 Å<sup>3</sup>/atom, which is close to the value of 6.995 Å<sup>3</sup>/atom for our 3800 K data, which can give some validity to the equations of state we have determined, and the methods used, as well as supporting our use of the EAM potential to define particle interactions. See Appendix E for the full use of the EOS formula, parameters, and thermal expansion.

## 2.5 – Iron–Silicon Melting Temperature

The melting temperature,  $T_m$ , is an important factor for when Equation 1 will be fit to the waiting time data as it defines the undercoolings that the points are plotted at along the X-axis, as well as being a parameter in Equation 1. Ideally, we would calculate the melting temperature of Fe–2.7 wt% Si ourselves and therefore use a constrained value to reduce the uncertainty, but the scope of this study does not allow for the calculation of this due to the difficulty of the

various methods. Therefore, we try to make an estimate of the melting temperature using two different methods, which provide upper and lower bounds and can be seen in Appendix F.

The main issue with the lower bound estimate is that the literature melting temperatures interpolated from are not well constrained, due to them being extrapolations of melting temperatures at much lower pressure conditions. We assume that the melting temperature decreases linearly following the best fit line of the melting temperature points. Furthermore, these studies are at much higher silicon concentrations than any values that have been proposed by studies of core composition, meaning that a big extrapolation is being made.

The problem with the upper bound estimate is that we have guessed the theoretically small discrepancy between the solid and liquid silicon concentrations when calculating its effect on the melting temperature, and we have not found any direct data on this, meaning that the value is not well constrained. We take the midpoint of these estimated upper and lower bounds due to their high uncertainties, giving us a melting temperature of  $6139 \pm 75$  K, which is a high range of error given that this is an important parameter in our calculation of the critical undercooling.

This melting temperature uncertainty puts uncertainty on which undercooled temperatures are being looked at. When taking a lower estimate, the 3 undercooling temperatures studied are in a similar range to those in the 2019 paper, but, when using a high melting temperature estimate, they shift to being slightly lower than the range used in Davies et al. (2019). Ideally, we want to be looking at undercooling values close enough to the melting temperature that the extrapolation in the critical undercooling value is reduced, but not too

high such that waiting times to observe freezing are too long, where the computation time increases greatly.

### 3. Results

#### 3.1 – Temperature and Pressure Data

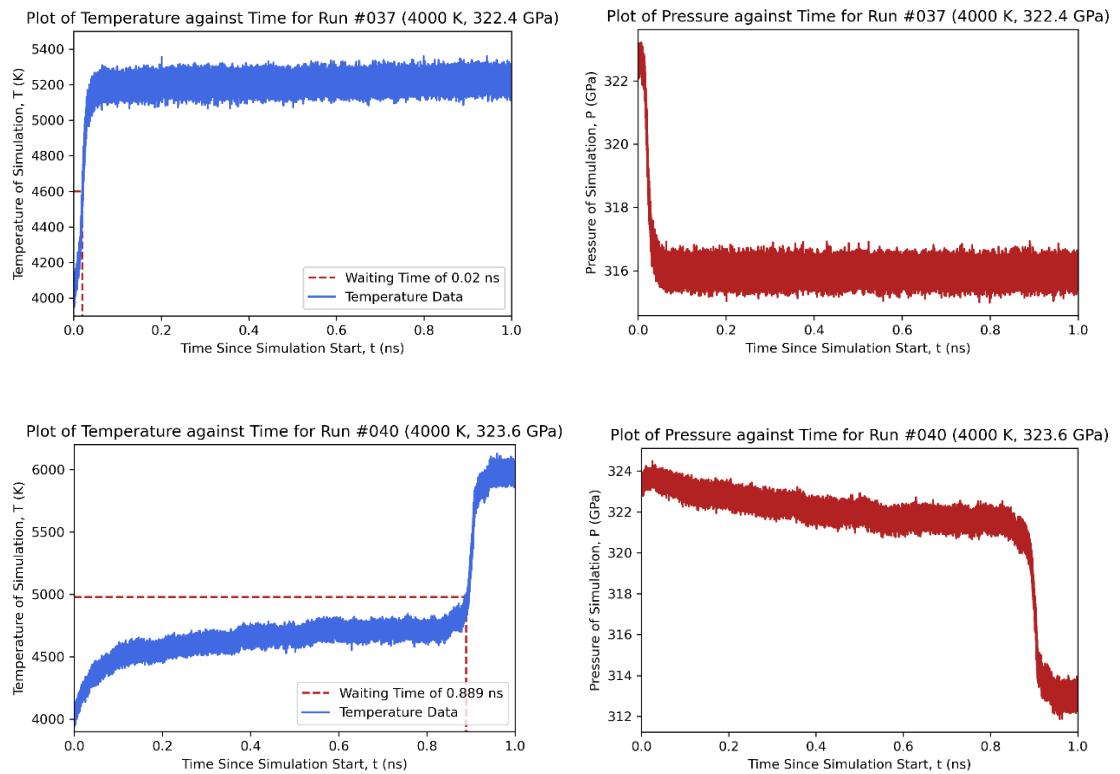


Figure 4 – Temperature and pressure against time at 4000K for the simulations that took the shortest and longest amounts of time to freeze, over the whole 1ns period. The red dashed line indicates the automatically calculated waiting time to freeze for these end members of the dataset. The changes in temperature are mirrored by the changes in pressure over time.

The waiting times to freeze for each simulation is automatically determined using a Python script. Latent heat releases when the system freezes due to a drop in pressure, causing a rapid temperature to increase that allows the measurements of waiting time to freeze to be made, which can be



seen in Figure 4 (Davies et al., 2019). The midpoint between the temperature averages of the first 50 and last 50 timesteps is used to give a corresponding waiting time that tends to lie in the middle of the sharp temperature increase. Even for simulations that take longer to freeze, the algorithm still chooses a point on the sharp increase, even if not in the middle, meaning all values should be relatively accurate, with this method allowing for automation of the data collection process.

Davies et al. (2019) correct their melting temperatures using a melting curve function due to the pressure of simulations varying by several GPa. However, for our data, this is not needed as for each temperature the equations of state provide the estimated ideal volumes that simulations are adjusted to. The uncertainties in the pressure data used to define the ideal volumes are small, meaning the pressures vary much less for each simulation. The average simulation pressures with error are  $322.9 \pm 0.3$ ,  $323.1 \pm 0.3$  and  $323.4 \pm 0.2$  for the 3800 K, 4000 K and 4200 K datasets respectively, meaning that our simulations are very close to the ideal pressure for the inner core boundary of 323 GPa, and verifying that our EOS is accurate.

### 3.2 – Average Waiting Times

The average waiting time for each temperature is calculated as

$$\tau_0 = \frac{1}{N_{frozen}} \sum_{j=1,50} \tau_x, \quad (3)$$

where  $\tau_x$  is the time taken for simulation  $x$  to freeze or the total simulation time if there is no freezing event within the specified time, and  $N_{frozen}$  is the number of simulations that successfully freeze, with an error bar of  $\sigma_0 = \tau_0 / \sqrt{N_{frozen}}$ ,

following the same calculation as Davies et al. (2019). The units of  $\tau_0$  are converted from ns to s and then these values are multiplied by simulation cell volumes  $V$  to give units of  $\text{sm}^3$  when plotted, which can be seen subsequently in Figure 6. ( $\tau_v = \tau_0 \times V$ ).

Using Equation 3 and including simulations that freeze rather than removing them from the data, rather than taking a simple mean average, means that simulations that did not freeze do not skew the data towards too low or too high waiting time values. For our simulations, all of them froze within the time of 1ns, so none were given a waiting time of 1ns and  $N_{frozen} = 50$ . An atomic density plot in Appendix Figure A3 shows that the ends of simulations have the structural uniformity of a frozen system. Some simulations did not reach 1 ns with certain initial configs, possibly due to the calculations randomly being more complex, and some others did not start due to random unexplained errors, so for both scenarios we discounted the data and ran new simulations, until 50 were successfully run.

### 3.3 – Atomic Structure

*Snapshots of a 3800K Run at Simulation Start and End*

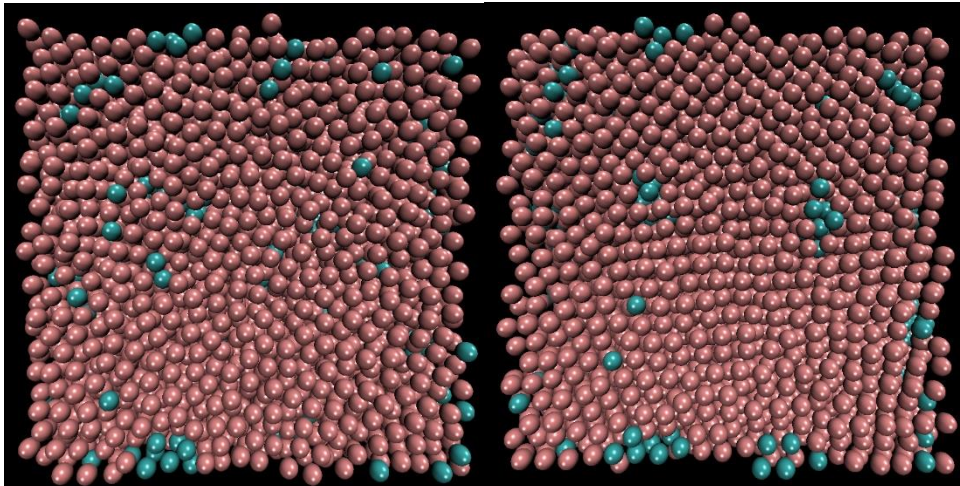


*Figure 5 – Snapshots of a 3800K simulation at the start (left image) and end (right image) of the 1ns period.*

Figure 5 gives a visual representation of the simulated boxes of iron and silicon atoms that we use in this study to look at freezing at undercooled temperatures and shows that the boxes of atoms give the structural appearance of freezing from solid to liquid material. The image from the start of the simulation appears to show a liquid, with the particles being arranged close together but in a random formation. The simulation end image shows a solid structure, with particles remaining close together, but being arranged in a much more regular way to give a fixed shape. Appendix Figure A2 shows this change of state through plots of Radial Distribution Functions.

### 3.4 – Critical Undercooling Results

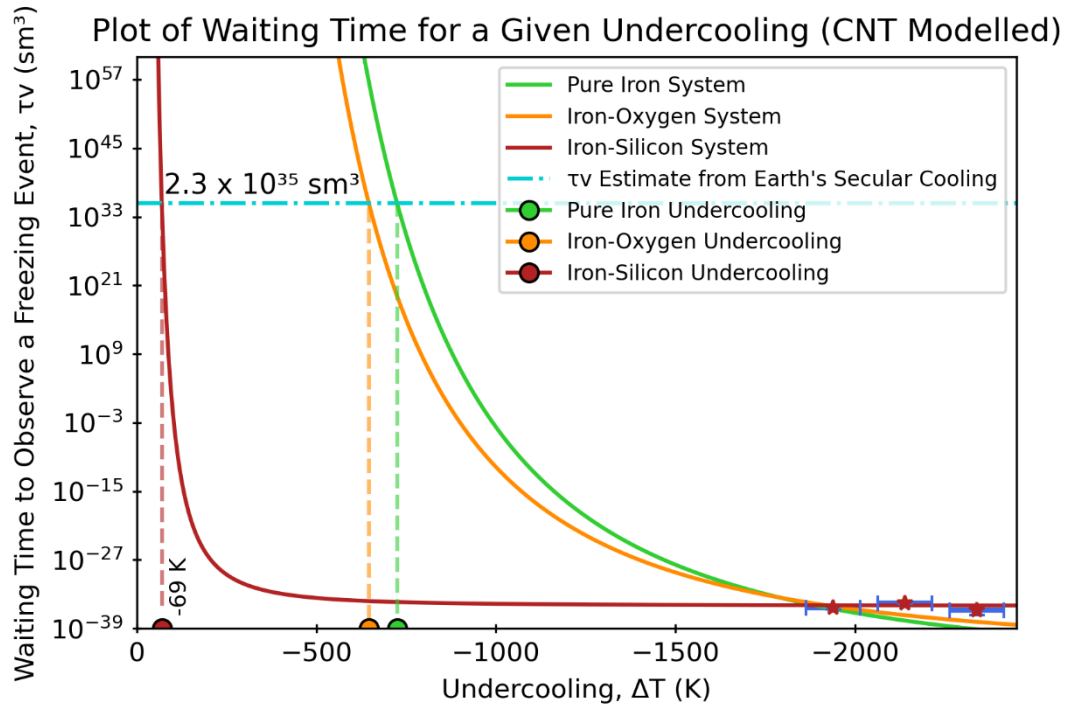


Figure 6a – Waiting time to observe freezing events against undercooling for the systems modelled by Davies et al. (2019), shown in orange and green, as well as the data from our Iron–Silicon system, shown in red. The red points are our waiting times plotted against their respective undercooling values with error bars, which are fitted to with Equation 1, using  $I_0$  and  $\gamma$  as free parameters, shown by the red curve. The dotted red line is the calculated required undercooling relevant to the inner core size and age, representing the undercooling at which the waiting time of the Iron–Silicon alloy equals  $2.3 \times 10^{35} \text{ sm}^3$ , shown with the blue dotted line.

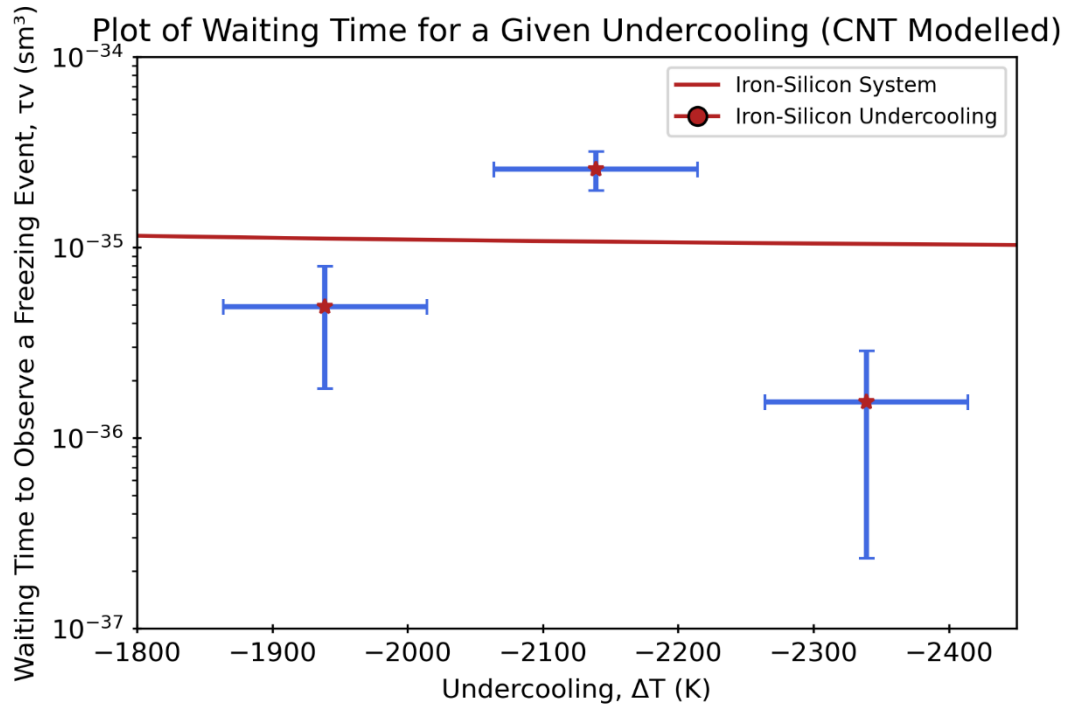
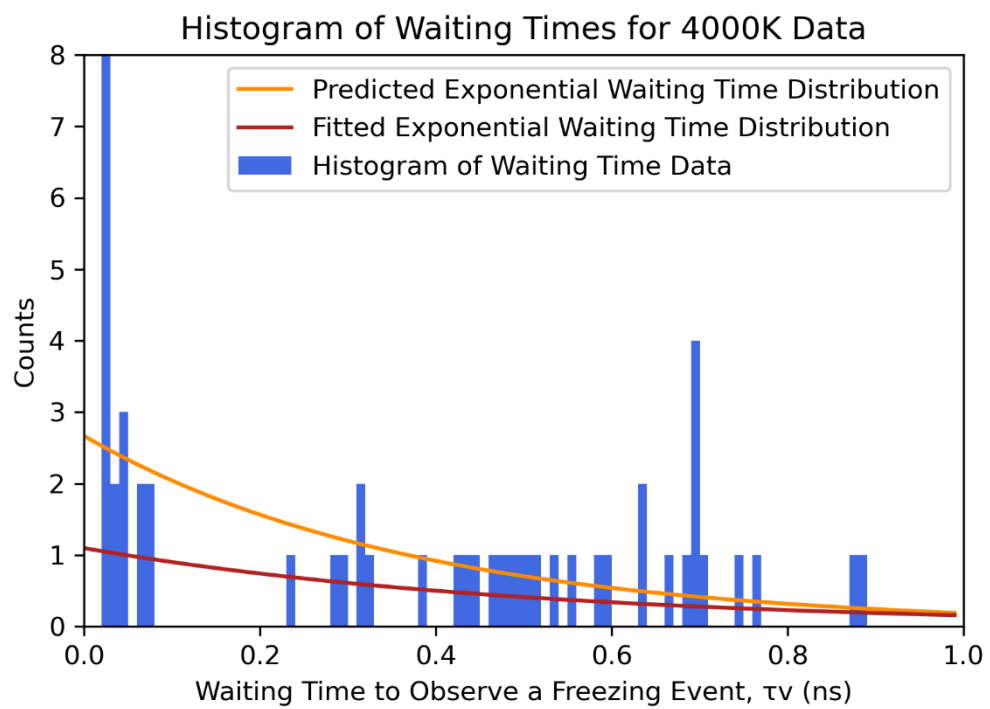
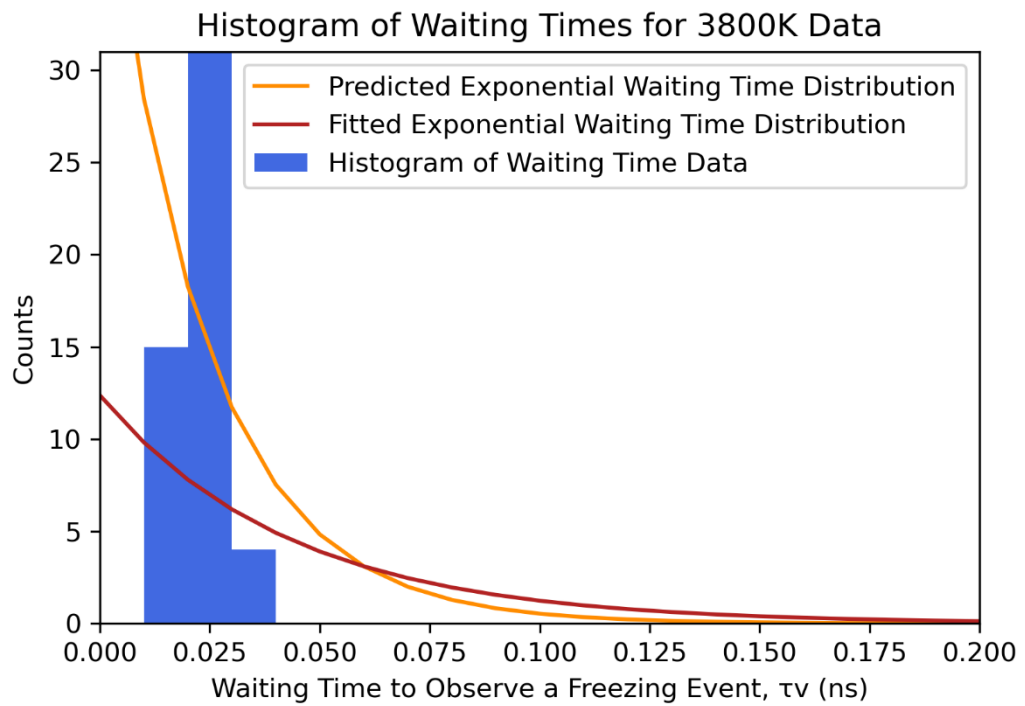


Figure 6b – Iron–Silicon waiting time points, shown in red with blue error bars, and the fit of Equation 1 to them, shown as a red line.

Figure 6 shows the average waiting time points plotted against undercooling, calculated using Equation 3 and converted to units of  $\text{sm}^3$ . The thermodynamic quantities  $I_0$  and  $\gamma$  are treated as free parameters in the fit of Equation 1 to the data, similarly to that in Davies et al. (2019). We obtain a final critical undercooling value of  $69 \pm 69$  K. The values of  $I_0$  and  $\gamma$  are found to be  $0.22 \pm 0.22$  and  $1.76 \pm 0.30 \times 10^{-35}$  respectively. See Appendix G for the calculation of the uncertainties and the raw data used.

### 3.5 – Distributions of the Data



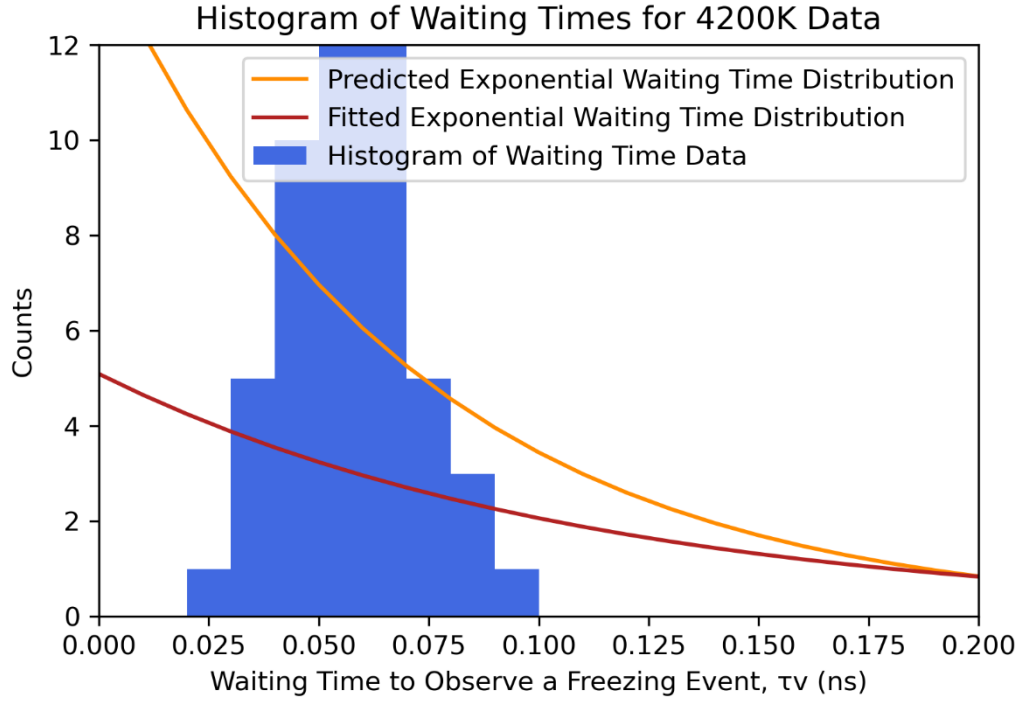


Figure 7 – Histograms of waiting time data with units of ns for 3800K, 4000K and 4200K datasets, shown in blue. Orange lines are the predicted exponential fit to the histogram data based in CNT whilst red lines are the actual best exponential fit to the histogram data. Histograms have 100 bins over the 1ns period, which gives a bin size of 0.01 ns. The 4200K histogram plot does not show all the data due to a single outlier that is at a much higher value, so we cut it out for visualisation purposes.

Figure 7 shows the histograms of the waiting time data for the three different temperature datasets. There is a gap at the start of the histograms where there are no low waiting times close to zero, which is a result of the waiting time algorithm mostly choosing the waiting time as the middle of the sharp increase, preventing instant waiting times from being recorded. There are similar gaps seen in the histograms of Davies et al. (2019), and it is possible that they exist for the same reasons. The distribution of waiting times is approximated by the exponential form  $\frac{1}{\tau_0 \exp\left[-\frac{\tau_v}{\tau_0}\right]}$  from CNT and can be seen by the orange lines in Figure 7.

## 4. Analysis and Discussion

### 4.1 – Uncertainties

Uncertainty in the average simulation pressure for each temperature comes from the standard deviation of the simulation pressures. Uncertainty in the EOS P–V data comes from the standard deviation of the 1000 pressure measurements and is very low, such that there is little uncertainty in the EOS fit and produces a negligible error bar in Figure 3.

Uncertainty in the critical undercooling comes from predefined vertical error bars ( $\sigma_0 = \tau_0 / \sqrt{N_{frozen}}$ ), the misfit between predicted and measured values for average waiting time based on analysis of the data histograms, and the uncertainty in the melting temperature (see Appendix G for the full calculation of these uncertainties) (Davies et al., 2019). These error bars are very large, meaning that the quality of the fit is not ideal, and the produced waiting time and histogram plots are not robust. In Figure 6b, although this is a log scale plot, the best fit line does not seem to be a good fit to the points, and there does not appear to be any clear trend to the points.

### 4.2 – Data Quality

The poor quality of the data can also be seen in Figure 7, as there appears to be a big disparity between the predicted exponential curve and the histograms, which do not seem to match this distribution at all. Even the fitted exponential to the data does not seem to match the trend of the data either, and fitting a reasonable distribution would require the use of a pre-factor or



normalisation of the data. CNT predicts that you should see an exponential distribution fit the data regardless of the size of the embryo, so the most obvious explanation why this has not occurred is that more data must be collected to “fill in” more of the histogram. The histograms support this, as the 4000 K distribution has a much larger spread of data whilst the 3800 K and 4200 K datasets show a much narrower spread that is clustered towards lower waiting times.

It was suggested from initial MD testing by members of the research team that 50 simulations were enough to see the exponential distribution, but perhaps quantities closer to those collected by Davies et al. (2019) would fix the problem, as they typically collected 128 simulations and saw a good match to the same distribution. The system size we use of 9826 atoms was chosen as previous testing by our research team members suggested that this system size is large enough such that freezing of the undercooled liquid can be easily observed. However, this may be too small and a larger system size of around 40000 atoms like that of Davies et al. (2019), might be necessary to show the behaviour that we are looking for. Also, another possibility is that we have collected enough values, but silicon changes the behaviour of iron enough such that the waiting time distribution is no longer fit by an exponential, although this is unlikely and further testing would be needed to confirm this.

### 4.3 – Thermodynamic Parameters

The consequences of the poor quality of the waiting time data and of the fit of Equation 1 has led to a great quantitative uncertainty in the critical undercooling,  $I_0$  and  $\gamma$  values. This casts doubt upon the validity of these results

and even though this data appears to show that the presence of silicon greatly requires the necessary undercooling for inner core nucleation, these great uncertainties and poor fit quality mean that a critical undercooling of  $69 \pm 69$  K cannot currently be accepted as a valid result. It is expected that alloying of silicon would at most lead to a similar reduction of the critical undercooling to oxygen as seen in Davies et al. (2019), so to show that there would be a reduction by hundreds of K is very difficult to believe, especially in context with the other results highlighted in Table 1. It is very plausible that the presence of silicon could be one of many steps towards resolving the paradox, but to say that it would essentially solve the paradox alone is something that must be determined when further testing is conducted.

The value of  $I_0$  is lower than the previous lowest calculated value by several orders of magnitude, although it is still a somewhat reasonable value as these different estimates all vary by several orders of magnitude (see Table 2). However, the value of  $\gamma$  is extremely low when compared to the values from these other studies, and it is not believable theoretically as the presence of silicon would have to greatly reduce the free interfacial energy between the solid and liquid material to achieve these values. When placing fixed constraints on these parameters in the fit of Equation 1 to be closer to the previous estimates meant that the fitting algorithm was unable to find a matching fit, which supports the lack of a trend supported by the theory.

#### 4.4 – Analysis of Methodology

There are effectively three ways of solving the paradox when following the DM simulation method, changing  $I_0$  or  $\gamma$ , or shifting the entire Equation 1

curve to smaller undercoolings. Changing  $I_0$  is unlikely to occur theoretically as it is a prefactor relating to embryo formation that is unlikely to change significantly, especially by the many orders of magnitude required to solve the paradox on its own. Reducing gamma  $\gamma$  to around 0.59 would be enough to give silicon alloying at least a value of 291K, which has an improbable chance of being low enough to solve the paradox. To try to shift the entire curve, we must constrain our data points to try and produce a statistically sound fit and exponentially distributed waiting time histogram.

In this study we have used a DM simulation method, like that of Davies et al. (2019), meaning that the limitations of that study also apply here. Namely, we are also using a “60 orders of magnitude” extrapolation and assuming that hcp iron is the nucleating phase. The works of Davies et al. (2019) and Wilson et al. (2021) have verified the validity of using CNT to extrapolate MD simulations to nucleation of the Earth’s core and make up the disparity in waiting times.

#### 4.5 – Investigating a Refit

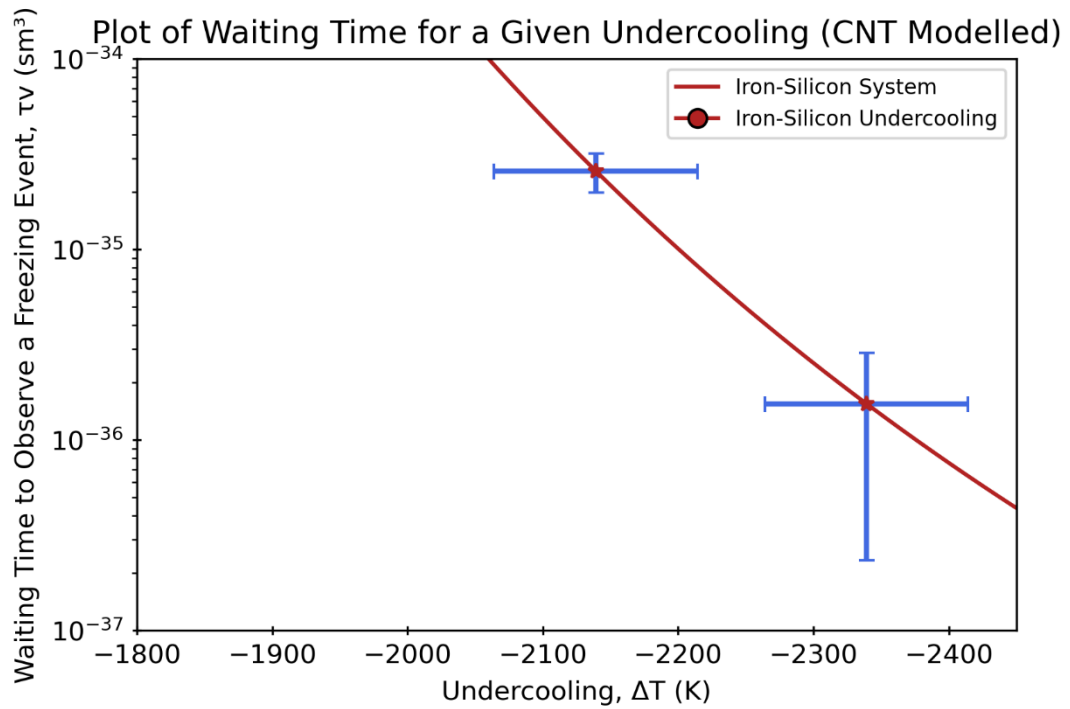
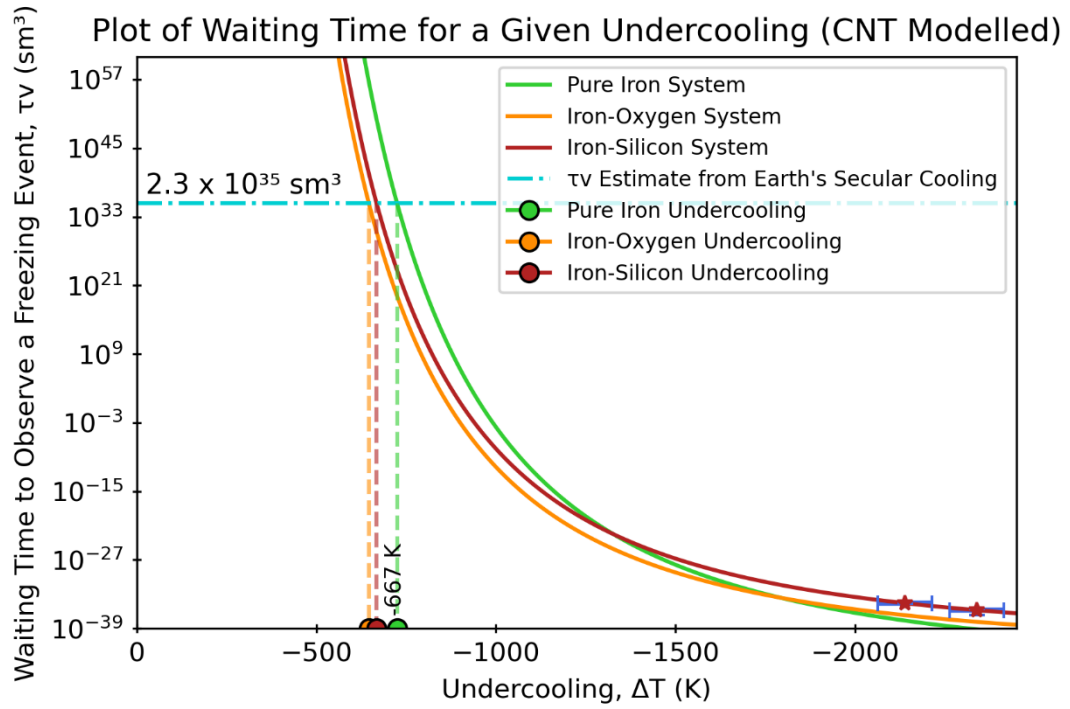


Figure 8 – Waiting time to observe freezing events against undercooling, with a fit of Equation 1 to the 2 lower temperature data points rather than to all 3.

To maximize the use of the collected data, we must consider again the points being fitted to. The highest temperature point should statistically be the most difficult to “fill” the histogram for, due to the longer waiting times predicted by CNT, meaning that this point might be the least constrained. Therefore, to investigate the possible effects of this, we refit to only the lower temperature points, as can be seen in Figure 8. This leads to a critical undercooling value of  $668 \pm 187$  K, which has a very large uncertainty window, but is much closer to the results of the previous studies seen in Table 1, especially to the value for iron–oxygen from Davies et al. (2019). This appears reasonable as it is foreseeable that these light elements with similar properties would have a similar thermodynamic effect when incorporated into iron. However, the uncertainty window is so large that we do not know if silicon might increase the critical undercooling over the value for pure iron found by Davies et al. (2019).

The  $I_0$  and  $\gamma$  values of  $1.01 \pm 0.22$  and  $1.09 \pm 1.09 \times 10^{-43}$  respectively are much more in line with the previous values, seen in Table 2, which is an improvement. When using this refit, despite the melting temperature uncertainty and the other uncertainties in the critical undercooling, silicon incorporation would not be enough to resolve the paradox alone, which is still a useful result. However, none of these conclusions made using this refit can be drawn as the data remains inconclusive, as it is not statistically justified to make a fit through only 2 data points, and we have no direct evidence to count any of these data points as anomalous results, so must consider them all.

#### 4.6 – Investigating the Available Undercooling

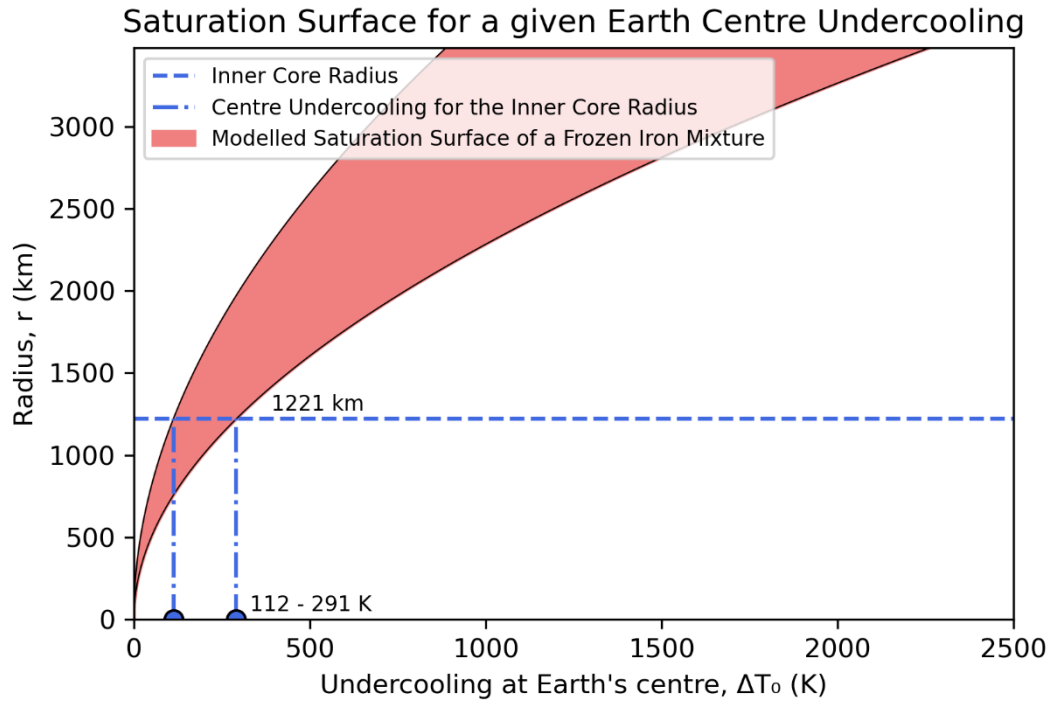


Figure 9 – Undercooling at Earth's centre as a function of undercooled layer radius using Appendix Equation H2. There is an uncertainty window which is a result of uncertainties of the various parameters, which can be seen in Appendix Table H1. The required undercooling values are found as the undercooling values which correspond to a saturation surface radius the same as that of the inner core boundary, and gives a minimum of 112 K and a maximum of 291 K.

There are some avenues through which the required undercooling can possibly be decreased. We have made an investigation into the undercooling available based on the current size of the inner core and following the method of Huguet et al. (2018), to see if a higher maximum undercooling than the value of ~200 K can be achieved, by using our own literature values for the various defining parameters, which can be seen in Appendix Table H1, along with their uncertainties. These have been used to plot Appendix Equation H2 as a function of  $r$ , which can be seen in Figure 9, with a maximum possible undercooling of 291 K based on the inner core radius being calculated, higher than the value calculated by Huguet et al. (2018). This can possibly give us a

smaller gap to close when trying to reduce the required inner core undercooling to a value that is appropriate to the inner core growth history. See Appendix H for a full list of the equations and parameters used.

However, the  $\sim 100\text{K/Gyr}$  cooling rate of the core since accretion is the other key factor that limits the available undercooling over the approximate 1 Gyr age of the core. A value of 291 K is not possible when considering this as the core is much too young. Further complicating this, reducing the critical undercooling to values even as low as  $\sim 10\text{ K}$  would also lead to a significant delay in the start of inner core crystallisation and impact on the core growth history, so ideally values must be brought down as close to 0 K as is possible to solve the problem in its entirety. This is within error of our calculated final value, but the invalidity of our results prevents us making use of this.

#### 4.7 – Homogeneous Solutions

We must also consider other routes that may reduce the homogeneous nucleation barrier. The predicted slurry layer above the core could affect the paradox by having a different temperature profile to a pure liquid, due to it effectively being a solid–liquid mixture (Wong et al, 2018). A large slurry layer would not instantly freeze when under the melting temperature, which would change the required undercooling.

A correlation has been proposed between external shock waves and accelerated nucleation following shock wave experiments on undercooled liquids, opening the potential for core pressure waves to have a similar effect, which has been tested by Davies et al. (2019) through the application of wave-like forcings to simulations (Ren et al., 2016). One avenue that has not yet been

investigated is the effects of magnetic fields in the core and their ability to cause these compression waves and shift the iron melting curve. However, Davies et al. (2019) find that this can only provide around ~100 K of undercooling, which means that this mechanism alone cannot solve the paradox.

Another option is to use an isothermal profile to define Appendix Equation H2 rather than an isotropic one to see if a higher maximum for available undercooling can be derived, as this has not been studied (Huguet et al., 2018). Similarly, the Lindemann melting curve is used to define Appendix Equation H2 but is not an exact profile, so a more accurate melting curve may be attainable with other methods. Making these theoretical adjustments may help to provide a small amount of undercooling but are highly unlikely to change the state of the paradox significantly.

## 4.8 – Heterogeneous Solutions

We have seen from the work of Davies et al. (2019) that homogeneous nucleation with pure iron and iron–oxygen do not solve the paradox, along with iron–silicon being unlikely to either, although we must conduct further studies on the latter. Therefore, heterogeneous nucleation must be considered as a possible solution to the problem. Davies et al. (2019) have demonstrated the greatly reduced nucleation barrier for heterogeneous nucleation through modelling simulations of nucleation with a solid seed, supporting the prediction by Shimizu et al. (2005) that inner core nucleation must begin heterogeneously. However, although heterogeneous nucleation on a solid substrate has a lower energy barrier and required undercooling than homogeneous nucleation,



scenarios in which this would be possible are unlikely and would lead to earlier and slower inner core growth (Huguet et al., 2018).

Huguet et al. (2018) present several possible substrates for heterogeneous nucleation, but the required circumstances are highly implausible, such that they are not currently reasonable solutions to the nucleation problem. For example, the least implausible scenario, a metal nugget entering the core from the mantle would have to firstly have high enough melting temperatures to remain solid in the core and be denser than the fluid outer core, leaving only metals such as gold and copper. These nuggets would have to have subducted into the deep mantle, and despite there being evidence for precipitation in the deep mantle of metallic iron phases such as those containing carbon and hydrogen, this has no bearing on the amount of gold, copper, or other viable metals in the deep mantle (Smith et al., 2016).

Even if these substances are present in the deep mantle, they would all tend to dissolve upon entering the core unless being of a large enough size, given as at least a ~9km radius in Huguet et al. (2018). The chances of this quantity of gold, copper or other viable metal being present in the deep mantle, even in other sources of iron alloys is almost negligible given the required circumstances, and the uncertainties are great, meaning that these situations are not worth exploring further unless new studies present very different circumstances.

## 4.9 – Future Work

We propose that future studies should focus on methods of reducing the barrier to homogeneous nucleation such as the MD methods we have utilised. A

range of iron–silicon concentrations should be investigated to see the effects on the required undercooling. For the collected points to potentially solve the paradox in the way they appear to show, the histogram must be “filled” with significantly more data points, at least 150 to be safe, and ideally at least five temperature points should be fit through rather than three, to reduce the uncertainties and verify or disprove the inconclusive results.

MD simulations should be conducted with some of the other main elements that core composition studies give to be in the core, such as sulphur, which is predicted to make up 1–2% of the core (Hirose et al., 2013). Constraining our results for silicon could also inform on the effect of sulphur on the nucleation barrier, as previous *ab initio* calculations show that sulphur and silicon partition almost equally between solids and liquids at conditions matching those during growth of the inner core (Alfè et al., 2002a; Davies et al., 2015).

Ideally, we would use a mixture of DM and PN simulation methods, for pure iron, iron–oxygen, iron–sulphur, and iron–silicon systems. The combination of these two methods removes some of the limitations of the individual methods we have discussed and allows for constraints to be placed on the critical undercooling for each of these mixtures by comparing the results from each method. It would be very useful to try simulating iron with multiple elements to simulate the actual inner core composition and its nucleation, but this is not very practical as the potentials are complex and lose their accuracy, with DFT being too expensive and slow to be utilised.

Furthermore, it is key that an accurate estimate of the iron–silicon melting temperature is calculated as this can help reduce the large uncertainties along with collecting more data. Possible methods that are related to the

molecular dynamics work of this study include estimates with MD data using the magnitudes of superheating and undercooling in the hysteresis method, the two-phase solid–liquid coexistence approach which looks at when the interface is observed to be stationary, and the z-method, which uses the relaxation temperature of the material following overheating of it until melting (Zhang et al., 2015). Other kinds of methods of calculation without using MD simulations include diamond anvil cell experiments with the fitting of thermodynamic equations, and ab initio experiments in DFT, using thermodynamic integration and calculating the solid and liquid free energies (Alfè et al, 2002b; Asanuma et al, 2010).

## 5. Conclusions

We have used a DM simulation method to collect data on the waiting time to freeze in iron–silicon alloys at inner core conditions for a range of undercooled temperatures, but the critical undercooling value of  $69 \pm 69$  K we have calculated is highly uncertain. We have been unable to make a statistically sound fit to the poor-quality data and constrain the CNT parameters to be at acceptable ranges. We cannot currently use our results to make clear interpretations about whether iron–silicon lowers the nucleation barrier or compare it directly to the pure iron and iron–oxygen systems investigated by Davies et al (2019).

However, this study does have some significance as, if the data points were constrained and uncertainties greatly reduced, our results suggest we may find that silicon is a useful substance in solving the nucleation paradox, but this remains to be seen. Further studies should use a mixture of DM and PN

simulation methods , for pure iron, iron–oxygen, iron–sulfur, and iron–silicon systems, to calculate the critical undercooling for each of these systems. They should aim to address the assumption that small nuclei energies can represent critical nuclei, and work towards solving the nucleation paradox, whilst also looking for mechanisms of homogeneous or heterogeneous nucleation that have not yet been considered.

## References

- Alder, B.J., Hoover, W.G., Young, D.A., 1968. Studies in Molecular Dynamics. V. High-Density EOS and Entropy for Hard Disks and Spheres. *The Journal of Chemical Physics* 49, 3688–3696. <https://doi.org/10.1063/1.1670653>
- Alfè, D., Gillan, M.J., Price, G.D., 2002a. Composition and temperature of the Earth's core constrained by combining ab initio calculations and seismic data. *Earth and Planetary Science Letters* 195, 91–98. [https://doi.org/10.1016/S0012-821X\(01\)00568-4](https://doi.org/10.1016/S0012-821X(01)00568-4)
- Alfè, D., Gillan, M.J., Price, G.D., 2002b. Complementary approaches to the ab initio calculation of melting properties. *The Journal of Chemical Physics* 116, 6170–6177. <https://doi.org/10.1063/1.1460865>
- Alfè, D., Gillan, M.J., Price, G.D., 2002c. Ab initio chemical potentials of solid and liquid solutions and the chemistry of the Earth's core. *The Journal of Chemical Physics* 116, 7127–7136. <https://doi.org/10.1063/1.1464121>
- Alfè, D., Price, G.D., Gillan, M.J., 2002d. Iron under Earth's core conditions: Liquid–state thermodynamics and high–pressure melting curve from ab initio calculations. *Phys. Rev. B* 65, 165118. <https://doi.org/10.1103/PhysRevB.65.165118>
- Allègre, C.J., Poirier, J.-P., Humler, E., Hofmann, A.W., 1995. The chemical composition of the Earth. *Earth and Planetary Science Letters* 134, 515–526. [https://doi.org/10.1016/0012-821X\(95\)00123-T](https://doi.org/10.1016/0012-821X(95)00123-T)
- Allen, M.P., 2004. Computational soft matter: from synthetic polymers to proteins. lect: Lecture notes, NIC series. NIC, Jülich.
- Anzellini, S., Dewaele, A., Mezouar, M., Loubeyre, P., Morard, G., 2013. Melting of Iron at Earth's Inner Core Boundary Based on Fast X-ray Diffraction. *Science* 340, 464–466. <https://doi.org/10.1126/science.1233514>

- Asanuma, H., Ohtani, E., Sakai, T., Terasaki, H., Kamada, S., Hirao, N., Sata, N., Ohishi, Y., 2008. Phase relations of Fe-Si alloy up to core conditions: Implications for the Earth inner core. *Geophysical Research Letters* 35. <https://doi.org/10.1029/2008GL033863>
- Asanuma, H., Ohtani, E., Sakai, T., Terasaki, H., Kamada, S., Kondo, T., Kikegawa, T., 2010. Melting of iron–silicon alloy up to the core–mantle boundary pressure: implications to the thermal structure of the Earth’s core. *Phys Chem Minerals* 37, 353–359. <https://doi.org/10.1007/s00269-009-0338-7>
- Badro, J., Aubert, J., Hirose, K., Nomura, R., Blanchard, I., Borensztajn, S., Siebert, J., 2018. Magnesium Partitioning Between Earth’s Mantle and Core and its Potential to Drive an Early Exsolution Geodynamo. *Geophys. Res. Lett.* 45. <https://doi.org/10.1029/2018GL080405>
- Badro, J., Fiquet, G., Guyot, F., Gregoryanz, E., Occelli, F., Antonangeli, D., d’Astuto, M., 2007. Effect of light elements on the sound velocities in solid iron: Implications for the composition of Earth’s core. *Earth and Planetary Science Letters* 254, 233–238. <https://doi.org/10.1016/j.epsl.2006.11.025>
- Badro, J., Siebert, J., Nimmo, F., 2016. An early geodynamo driven by exsolution of mantle components from Earth’s core. *Nature* 536, 326–328. <https://doi.org/10.1038/nature18594>
- Belonoshko, A.B., Ahuja, R., Johansson, B., 2003. Stability of the body–centred–cubic phase of iron in the Earth’s inner core. *Nature* 424, 1032–1034. <https://doi.org/10.1038/nature01954>
- Belonoshko, A.B., Lukinov, T., Fu, J., Zhao, J., Davis, S., Simak, S.I., 2017. Stabilization of body–centred cubic iron under inner–core conditions. *Nature Geosci* 10, 312–316. <https://doi.org/10.1038/ngeo2892>
- Chen, B., Gao, L., Funakoshi, K., Li, J., 2007. Thermal expansion of iron–rich alloys and implications for the Earth’s core. *Proc. Natl. Acad. Sci. U.S.A.* 104, 9162–9167. <https://doi.org/10.1073/pnas.0610474104>
- Christian, J.W., 2002. The Classical Theory of Nucleation, in: *The Theory of Transformations in Metals and Alloys*. Elsevier, pp. 422–479. <https://doi.org/10.1016/B978-008044019-4/50014-3>
- Côté, A.S., Vočadlo, L., Brodholt, J.P., 2008. The effect of silicon impurities on the phase diagram of iron and possible implications for the Earth’s core structure. *Journal of Physics and Chemistry of Solids* 69, 2177–2181. <https://doi.org/10.1016/j.jpcs.2008.03.031>
- Davies, C., Pozzo, M., Gubbins, D., Alfè, D., 2015. Constraints from material properties on the dynamics and evolution of Earth’s core. *Nature Geosci* 8, 678–685. <https://doi.org/10.1038/ngeo2492>

- Davies, C.J., 2015. Cooling history of Earth's core with high thermal conductivity. *Physics of the Earth and Planetary Interiors* 247, 65–79. <https://doi.org/10.1016/j.pepi.2015.03.007>
- Davies, C.J., Pozzo, M., Alfè, D., 2019. Assessing the inner core nucleation paradox with atomic-scale simulations. *Earth and Planetary Science Letters* 507, 1–9. <https://doi.org/10.1016/j.epsl.2018.11.019>
- Daw, M.S., 1989. Model of metallic cohesion: The embedded-atom method. *Phys. Rev. B* 39, 7441–7452. <https://doi.org/10.1103/PhysRevB.39.7441>
- Daw, M.S., Baskes, M.I., 1983. Semiempirical, Quantum Mechanical Calculation of Hydrogen Embrittlement in Metals. *Phys. Rev. Lett.* 50, 1285–1288. <https://doi.org/10.1103/PhysRevLett.50.1285>
- Dye, S.T., 2010. Geo-neutrinos and silicate earth enrichment of U and Th. *Earth and Planetary Science Letters* 297, 1–9. <https://doi.org/10.1016/j.epsl.2010.06.012>
- Dziewonski, A.M., Anderson, D.L., 1981. Preliminary reference Earth model. *Physics of the Earth and Planetary Interiors* 25, 297–356. [https://doi.org/10.1016/0031-9201\(81\)90046-7](https://doi.org/10.1016/0031-9201(81)90046-7)
- Edmund, E., Antonangeli, D., Decremps, F., Miozzi, F., Morard, G., Boulard, E., Clark, A.N., Ayrinhac, S., Gauthier, M., Morand, M., Mezouar, M., 2019. Velocity-Density Systematics of Fe-5wt%Si: Constraints on Si Content in the Earth's Inner Core. *Journal of Geophysical Research: Solid Earth* 124, 3436–3447. <https://doi.org/10.1029/2018JB016904>
- Fischer, R.A., Campbell, A.J., Caracas, R., Reaman, D.M., Heinz, D.L., Dera, P., Prakapenka, V.B., 2014. Equations of state in the Fe-FeSi system at high pressures and temperatures. *J. Geophys. Res. Solid Earth* 119, 2810–2827. <https://doi.org/10.1002/2013JB010898>
- Fischer, R.A., Campbell, A.J., Reaman, D.M., Miller, N.A., Heinz, D.L., Dera, P., Prakapenka, V.B., 2013. Phase relations in the Fe-FeSi system at high pressures and temperatures. *Earth and Planetary Science Letters* 373, 54–64. <https://doi.org/10.1016/j.epsl.2013.04.035>
- Gomi, H., Ohta, K., Hirose, K., Labrosse, S., Caracas, R., Verstraete, M.J., Hernlund, J.W., 2013. The high conductivity of iron and thermal evolution of the Earth's core. *Physics of the Earth and Planetary Interiors* 224, 88–103. <https://doi.org/10.1016/j.pepi.2013.07.010>
- Gubbins, D., 1977. Energetics of the Earth's core. *J Geophys* 43, 453–464.
- Gubbins, D., Alfè, D., Masters, G., Price, G.D., Gillan, M.J., 2003. Can the Earth's dynamo run on heat alone? *Geophysical Journal International* 155, 609–622. <https://doi.org/10.1046/j.1365-246X.2003.02064.x>

- Gubbins, D., Alfè, D., Davies, C., Pozzo, M., 2015. On core convection and the geodynamo: Effects of high electrical and thermal conductivity. *Physics of the Earth and Planetary Interiors* 247, 56–64.  
<https://doi.org/10.1016/j.pepi.2015.04.002>
- Hirao, N., Ohtani, E., Kondo, T., Kikegawa, T., 2004. EOS of iron–silicon alloys to megabar pressure. *Phys Chem Minerals* 31.  
<https://doi.org/10.1007/s00269-004-0387-x>
- Hirose, K., Labrosse, S., Hernlund, J., 2013. Composition and State of the Core. *Annu. Rev. Earth Planet. Sci.* 41, 657–691.  
<https://doi.org/10.1146/annurev-earth-050212-124007>
- Hirose, K., Morard, G., Sinmyo, R., Umemoto, K., Hernlund, J., Helffrich, G., Labrosse, S., 2017. Crystallization of silicon dioxide and compositional evolution of the Earth’s core. *Nature* 543, 99–102.  
<https://doi.org/10.1038/nature21367>
- Huguet, L., Van Orman, J.A., Hauck, S.A., Willard, M.A., 2018. Earth’s inner core nucleation paradox. *Earth and Planetary Science Letters* 487, 9–20.  
<https://doi.org/10.1016/j.epsl.2018.01.018>
- Kelton, K.F., Lee, G.W., Gangopadhyay, A.K., Hyers, R.W., Rathz, T.J., Rogers, J.R., Robinson, M.B., Robinson, D.S., 2003. First X-Ray Scattering Studies on Electrostatically Levitated Metallic Liquids: Demonstrated Influence of Local Icosahedral Order on the Nucleation Barrier. *Phys. Rev. Lett.* 90, 195504.  
<https://doi.org/10.1103/PhysRevLett.90.195504>
- Labrosse, S., 2015. Thermal evolution of the core with a high thermal conductivity. *Physics of the Earth and Planetary Interiors* 247, 36–55.  
<https://doi.org/10.1016/j.pepi.2015.02.002>
- Labrosse, S., Macouin, M., 2002. The inner core and the geodynamo. *Comptes Rendus Geoscience* 335, 37–50. [https://doi.org/10.1016/S1631-0713\(03\)00013-0](https://doi.org/10.1016/S1631-0713(03)00013-0)
- Labrosse, S., Poirier, J.-P., Le Mouél, J.-L., 1996. On cooling of the Earth’s core. *Physics of the Earth and Planetary Interiors* 99, 1–17.  
[https://doi.org/10.1016/S0031-9201\(96\)03207-4](https://doi.org/10.1016/S0031-9201(96)03207-4)
- Lasbleis, M., Kervazo, M., Choblet, G., 2019. The Fate of Liquids Trapped During the Earth’s Inner Core Growth. *Geophys. Res. Lett.* 47.  
<https://doi.org/10.1029/2019GL085654>
- Lin, J.-F., Campbell, A.J., Heinz, D.L., Shen, G., 2003. Static compression of iron-silicon alloys: Implications for silicon in the Earth’s core. *Journal of Geophysical Research: Solid Earth* 108.  
<https://doi.org/10.1029/2002JB001978>

- Lord, O.T., Walter, M.J., Dobson, D.P., Armstrong, L., Clark, S.M., Kleppe, A., 2010. The FeSi phase diagram to 150 GPa. *J. Geophys. Res.* 115, B06208. <https://doi.org/10.1029/2009JB006528>
- Nimmo, F., 2015. Energetics of the Core.
- O'Rourke, J.G., Stevenson, D.J., 2016. Powering Earth's dynamo with magnesium precipitation from the core. *Nature* 529, 387–389. <https://doi.org/10.1038/nature16495>
- Pozzo, M., Davies, C., Gubbins, D., Alfè, D., 2012. Thermal and electrical conductivity of iron at Earth's core conditions. *Nature* 485, 355–358. <https://doi.org/10.1038/nature11031>
- Ren, Y., Lee, J., Hutchins, K.M., Sottos, N.R., Moore, J.S., 2016. Crystal Structure, Thermal Properties, and Shock–Wave–Induced Nucleation of 1,2–Bis(phenylethynyl)benzene. *Crystal Growth & Design* 16, 6148–6151. <https://doi.org/10.1021/acs.cgd.6b01119>
- Roberts, P.H., Glatzmaier, G.A., 2000. Geodynamo theory and simulations. *Rev. Mod. Phys.* 72, 1081–1123. <https://doi.org/10.1103/RevModPhys.72.1081>
- Shahar, A., Ziegler, K., Young, E.D., Ricolleau, A., Schauble, E.A., Fei, Y., 2009. Experimentally determined Si isotope fractionation between silicate and Fe metal and implications for Earth's core formation. *Earth and Planetary Science Letters* 288, 228–234. <https://doi.org/10.1016/j.epsl.2009.09.025>
- Shimizu, H., Poirier, J.P., Le Mouél, J.L., 2005. On crystallization at the inner core boundary. *Physics of the Earth and Planetary Interiors* 151, 37–51. <https://doi.org/10.1016/j.pepi.2005.01.001>
- Smith, E.M., Shirey, S.B., Nestola, F., Bullock, E.S., Wang, J., Richardson, S.H., Wang, W., 2016. Large gem diamonds from metallic liquid in Earth's deep mantle. *Science* 354, 1403–1405. <https://doi.org/10.1126/science.aal1303>
- Stacey, F.D., 1993. Thermodynamics relationships and the properties of iron at earth's core conditions, in: Conference proceedings for the Association for the International Advancement of High Pressure Colorado Springs, Colorado.
- Sun, Y., Zhang, F., Mendeleev, M., Wentzcovitch, R., Ho, K., 2022. Two-step nucleation of the Earth's inner core. *Proceedings of the National Academy of Sciences*. <https://doi.org/10.1073/pnas.2113059119>
- Sutton, A.P., Chen, J., 1990. Long–range Finnis–Sinclair potentials. *Philosophical Magazine Letters* 61, 139–146. <https://doi.org/10.1080/09500839008206493>



- Takafuji, N., 2005. Solubilities of O and Si in liquid iron in equilibrium with (Mg,Fe)SiO<sub>3</sub> perovskite and the light elements in the core. *Geophys. Res. Lett.* 32, L06313. <https://doi.org/10.1029/2005GL022773>
- Tarduno, J.A., Blackman, E.G., Mamajek, E.E., 2014. Detecting the oldest geodynamo and attendant shielding from the solar wind: Implications for habitability. *Physics of the Earth and Planetary Interiors* 233, 68–87. <https://doi.org/10.1016/j.pepi.2014.05.007>
- Tarduno, J.A., Cottrell, R.D., Watkeys, M.K., Hofmann, A., Doubrovine, P.V., Mamajek, E.E., Liu, D., Sibeck, D.G., Neukirch, L.P., Usui, Y., 2010. Geodynamo, Solar Wind, and Magnetopause 3.4 to 3.45 Billion Years Ago. *Science* 327, 1238–1240. <https://doi.org/10.1126/science.1183445>
- Tateno, S., Kuwayama, Y., Hirose, K., Ohishi, Y., 2015. The structure of Fe–Si alloy in Earth’s inner core. *Earth and Planetary Science Letters* 418, 11–19. <https://doi.org/10.1016/j.epsl.2015.02.008>
- Tsuchiya, T., Fujibuchi, M., 2009. Effects of Si on the elastic property of Fe at Earth’s inner core pressures: First principles study. *Physics of the Earth and Planetary Interiors* 174, 212–219. <https://doi.org/10.1016/j.pepi.2009.01.007>
- Turnbull, D., 1950. Formation of Crystal Nuclei in Liquid Metals. *Journal of Applied Physics* 21, 1022–1028. <https://doi.org/10.1063/1.1699435>
- Wilson, A.J., Walker, A.M., Alfè, D., Davies, C.J., 2021. Probing the nucleation of iron in Earth’s core using molecular dynamics simulations of undercooled liquids. *Phys. Rev. B* 103, 214113. <https://doi.org/10.1103/PhysRevB.103.214113>
- Wong, J., Davies, C.J., Jones, C.A., 2018. A Boussinesq slurry model of the F–layer at the base of Earth’s outer core. *Geophysical Journal International* 214, 2236–2249. <https://doi.org/10.1093/gji/ggy245>
- Zhang, W.–J., Liu, Z.–Y., Liu, Z.–L., Cai, L.–C., 2015. Melting curves and entropy of melting of iron under Earth’s core conditions. *Physics of the Earth and Planetary Interiors* 244, 69–77. <https://doi.org/10.1016/j.pepi.2014.10.011>
- Ziegler, K., Young, E.D., Schauble, E.A., Wasson, J.T., 2010. Metal–silicate silicon isotope fractionation in enstatite meteorites and constraints on Earth’s core formation. *Earth and Planetary Science Letters* 295, 487–496. <https://doi.org/10.1016/j.epsl.2010.04.030>

## Appendices

## Section A – Supplementary Plots

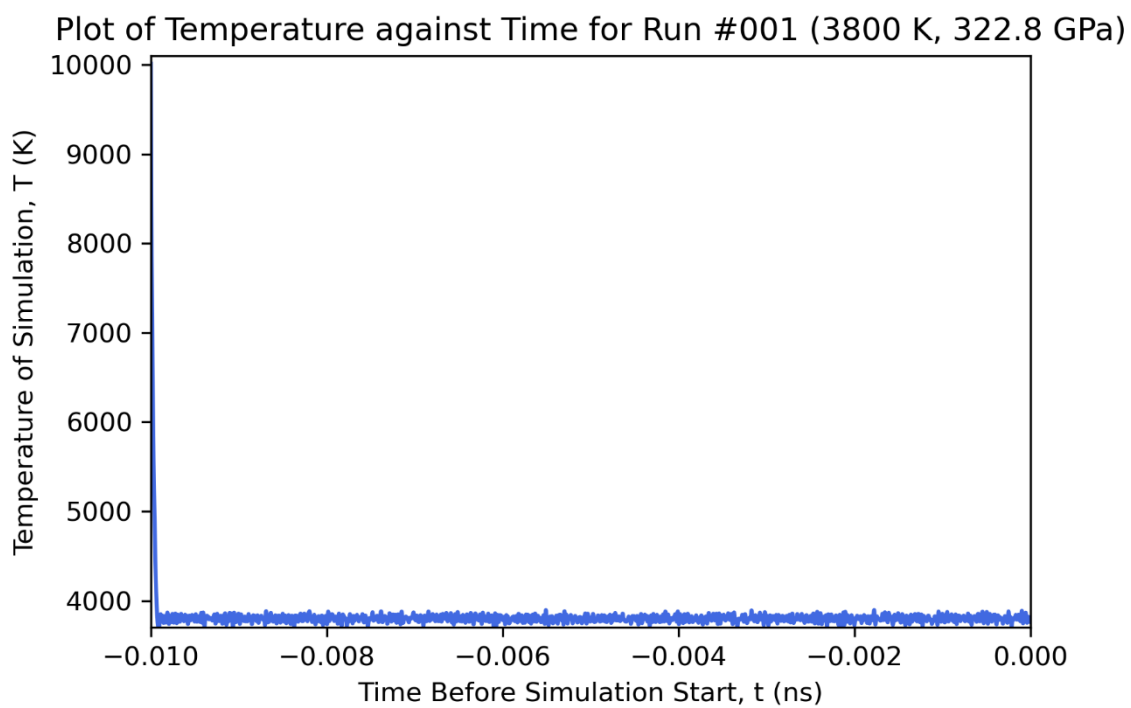


Figure A1 – 10000-step equilibration of the system in NVT for a 3800 K run.

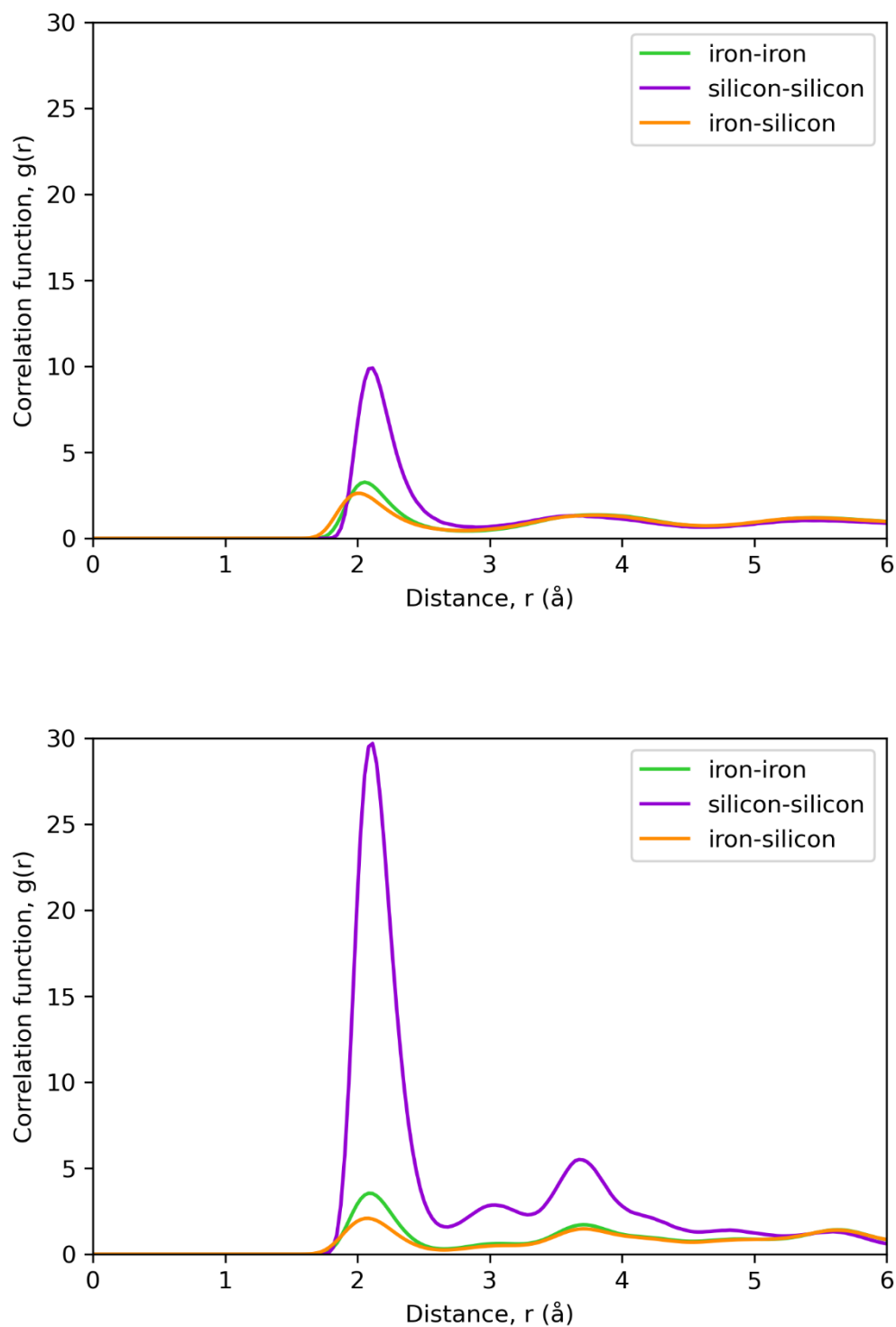


Figure A2 – Radial Distribution Function plots of correlation function against atomic distance at the start (top plot) and end (bottom plot) of the 1ns period of a single run for the 3 different pair potentials. A change of state can be seen over this period, as the RDF from the simulation start shows the characteristic sharp peak followed by much smaller peaks seen in liquids, whilst the end RDF shows the traits of a solid, with broadened discrete peaks that represent coordinate shells.

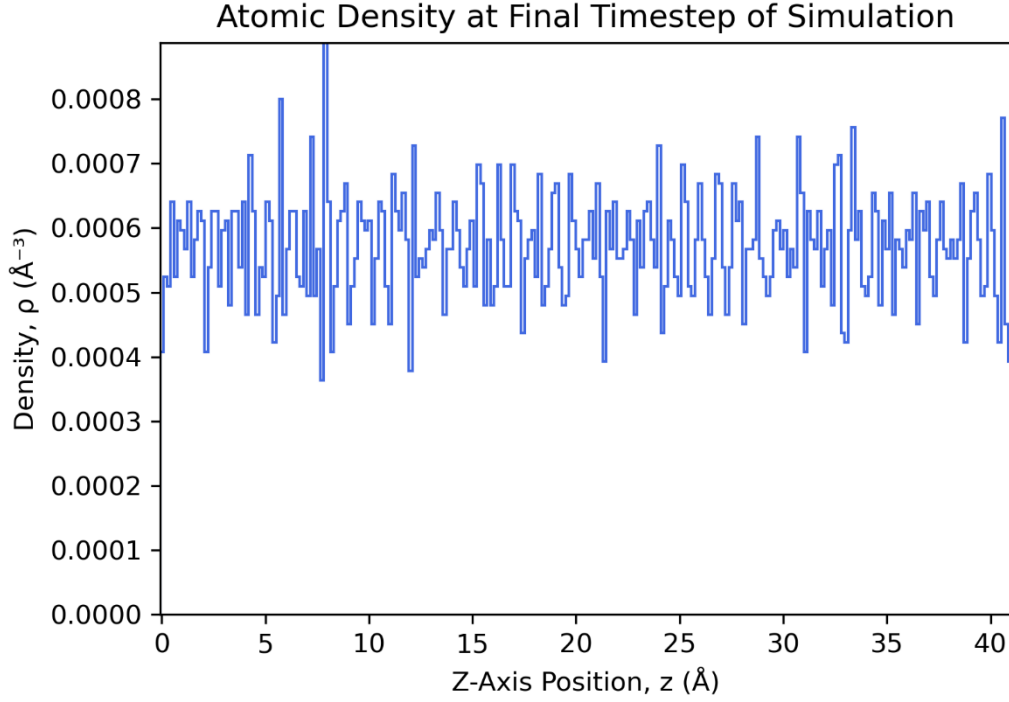


Figure A3 – 1-dimensional atomic density at the end of the 1 ns simulation period for a single run. The atomic density is roughly uniform across the entire length, which evidences the system is frozen.

## Section B – CNT Derivations

Following on from Equation 2, the number of embryos formed per unit volume

per unit time,  $I$ , is proportional to  $\exp\left(-\frac{\Delta G}{k_B T}\right)$ , by approximating the first

exponential in the CNT exponential law of the formation rate of nuclei with the

critical radius. Setting  $\frac{d\Delta G}{dr} = 0$  leads to  $r_c = -\frac{2\gamma}{g_{SL}}$ . The difference in free energies

between the solid and liquid can be defined as

$$g_{SL} \approx h_f \frac{\Delta T}{T_m} h_c. \quad (\text{B1})$$

The critical radius beyond which a nucleus can grow without remelting is

therefore rewritten as

$$r_c \approx \frac{2\gamma T_m}{h_f h_c \Delta T_c}. \quad (\text{B2})$$

The height of the nucleation energy barrier is found by substituting equations (B1) and (B2) into Equation 2, and is therefore defined as

$$\Delta G_c = \frac{16\pi\gamma^3 T_m^2}{3\Delta T_c^2 h_f^2 h_c^2}. \quad (B3)$$

The number of embryos reaching the critical radius  $r_c$  per unit volume per unit time is found by substituting Equation B3 into  $\exp\left(-\frac{\Delta G}{k_B T}\right)$  and given as

$$I = I_0 \exp\left[-\frac{16\pi\gamma^3 T_m^2}{3k_B T \Delta T_c^2 h_f^2 h_c^2}\right]. \quad (B4)$$

The average waiting time to observe a freezing event is the average time elapsed until freezing of an undercooling liquid is seen. At the top of the nucleation energy barrier, on average half of the embryos will grow and lead to a freezing event whilst the other half will remelt, leading to Equation 1.

### Section C – EAM Equations

Material	$\epsilon$ (eV)	$a$ (Å)	N	m	$C$
Fe	0.1662	3.4714	5.93	4.788	16.55
Si	0.371367	2.548654	9.309811	7.087163	13.12957
Fe–Si	0.348938	3.307381	5.148793	4.644531	

*Table C1 – EAM parameters used in equations (C1–6) to define potentials between different atom combinations.*

The EAM potential we use is one developed in Alfè et al. (2002b) like those used in Davies et al. (2019), and of the form

$$E_{tot} = \sum_{i_{Fe}} E_{i_{Fe}} + \sum_{i_{Si}} E_{i_{Si}} + \sum_{i_{FeSi}} E_{i_{FeSi}}, \quad (C1)$$

where  $i_{Fe}$  sums over the iron atoms,  $i_{Si}$  sums over the silicon atoms and  $i_{FeSi}$  sums over all the atoms. The atomic energies are defined as

$$E_{i_{Fe}} = E_{i_{Fe}}^{rep} + F_{Fe}(\rho_{i_{Fe}}) = \sum_{i < j} \epsilon_{Fe} (a_{Fe}/r_{i_{Fe}j_{Fe}})^{n_{Fe}} - \epsilon_{Fe} C_{Fe} \rho_{i_{Fe}}^{1/2}, \quad (C2)$$

$$E_{i_{Si}} = E_{i_{Si}}^{rep} + F_{Si}(\rho_{i_{Si}}) = \sum_{i < j} \epsilon_{Si} (a_{Si}/r_{i_{Si}j_{Si}})^{n_{Si}} - \epsilon_{Si} C_{Si} \rho_{i_{Si}}^{1/2}, \quad (C3)$$

and

$$E_{i_{FeSi}} = E_{i_{FeSi}}^{rep} = 1/2 \sum_{i_{Fe} \neq j_{Si}} \epsilon_{FeSi} (a_{FeSi}/r_{i_{FeSi}j_{FeSi}})^{n_{FeSi}}, \quad (C4)$$

with densities of

$$\rho_{i_{Fe}} = \sum_{j_{Fe} \neq i_{Fe}} (a_{Fe}/r_{i_{Fe}j_{Fe}})^{m_{Fe}} + \sum_{j_{Si}} (a_{FeSi}/r_{i_{Fe}j_{Si}})^{m_{FeSi}} \quad (C5)$$

and

$$\rho_{i_{Si}} = \sum_{j_{Si} \neq i_{Si}} (a_{Si}/r_{i_{Si}j_{Si}})^{m_{Si}} + \sum_{i_{Fe}} (a_{FeSi}/r_{i_{Fe}i_{Si}})^{m_{FeSi}}, \quad (C6)$$

where  $E^{rep}$  is a purely repulsive function of interatomic distances  $r_{ij}$  along with  $F(\rho_i)$  as an embedding term to account for metallic bonding.

## Section D – Details of LAMMPS Simulations

The Verlet algorithm is utilised to integrate the Newtonian equations of motion to calculate particle trajectories and their movement through the system, providing time reversibility and keeping the dynamics explicit, and allowing steps to be undone such that events can be repeated or altered. This is the standard method used in MD and does not have any additional computational cost to other, more simple methods. A 1 fs timestep is used in the simulations,

which is the standard value for MD simulations to maximize efficiency. This is the largest timestep that produces stable dynamics. Thermodynamic quantities such as temperature, pressure and total energy are extracted at every timestep.

Parameter	Value
units	metal
atom_style	atomic
dimension	3
boundary	p p p

*Table D1 – LAMMPS code parameters used to setup boxes of atoms*

Three-dimensional boxes of atoms are setup with default atomic attributes for coarse-grained liquids, solids and metals modelled as point particles, relevant to the atoms we are studying. The box is periodic in all three dimensions, meaning that particles interact across the boundary and can travel from one side to the other instantaneously, to approximate the much larger size of the inner core. The parameters to achieve these conditions can be seen in Table D1. These systems are comprised of 9826 atoms, split up into 9320 iron atoms and 506 silicon atoms, and giving the chosen wt% silicon of 2.7%.

The system is be started with the 9826 iron atoms at a relatively low temperature of 3000 K and progressively moves up to 10000 K over 5000 timesteps to melt the system and form a pure liquid. The NVT ensemble, with constant number of particles N, volume V and absolute temperature T, keeps energies stable and at relevant values and makes particle behaviour more visible. The system is stopped, 502 atoms are randomly transmuted to iron to remove any effects on the change of state in the iron, and then it is restarted

with new velocities drawn from a random Maxwellian distribution to remove energy “leftover” from the previous step, still being within the NVT canonical ensemble. The system is held at the goal temperature, below the melting temperature, for 10000 timesteps to equilibrate the system and tend towards the temperature of interest. After this is the main part of the simulation, which is run for 1 ns. The system is restarted with new random Maxwellian velocities, and a switch is made to the NVE microcanonical ensemble, with constant total energy rather than constant absolute temperature, which allows for the system to undergo freezing if nucleation occurs.

### Example LAMMPS Script

```
#####
variable      TOT_TIME      equal 1000000 # run simulation for # timesteps in total
variable      TEMPERATURE equal 9999.9 # Temperature

##### Box #####

units          metal
atom_style     atomic
dimension      3
boundary       p p p

read_data      thermalised.data
variable      Fe equal 1
variable      Si equal 2

##### Potential #####
pair_style     eam/fs
pair_coeff     * * Fe_Si_eam.fs Fe Si
neighbor       0.5 bin
neigh_modify   every 1 delay 5 check yes

##### Ensemble #####

thermo_style   custom step time temp pe ke etotal press
thermo         1

variable      timeVals equal time+15
variable      tempVals equal temp
variable      potVals equal pe
variable      kinVals equal ke
variable      energyVals equal etotal
variable      pressVals equal press

fix           1 all print 1 "${timeVals} ${tempVals} ${potVals} ${kinVals} ${energyVals} ${pressVals}" append thermodata.txt
velocity      all create ${TEMPERATURE} 11111 loop geom
fix           2 all nve

timestep      0.001 # in ps. so 0.5 ns for now
run_style     verlet

dump          7 all custom 100 step3.pos.lammps id type x y z
dump_modify   7 sort id

compute       gofr all rdf 500 1 1 2 2 1 2
fix           rdf all ave/time 1 10000 10000 c_gofr[*] file rdf3.txt mode vector

run ${TOT_TIME}
```

Figure D2 – Example LAMMPS script used in the 1ns NVE part of the simulation.

## Section E – Equations of State and Thermal Expansion



Temperature	wt% Si	$V_0$	$B_0$	$B'_0$	Ideal Volume (Å <sup>3</sup> /atom)	Ideal Volume (m <sup>3</sup> )
3800 K	2.7	6.997	215.1	9.130	6.995	6.873 x 10 <sup>-26</sup>
4000 K	2.7	6.816	245.5	8.704	7.007	6.885 x 10 <sup>-26</sup>
4200 K	2.7	6.568	294.5	8.536	7.017	6.895 x 10 <sup>-26</sup>

Table E1a – Birch–Murnaghan parameters for fitted data and calculated ideal volumes at 323 GPa for three different temperatures shown in Figure 3

Original Temperature	wt% Si	Source	$V_0$	$V_0^{3800}$	$B_0$	$B'_0$	$\alpha^{init}$	Ideal Volume (Å <sup>3</sup> /atom)
300 K	9	Fischer et al. (2014)	7.203	7.969	129.1	5.29	4.899 x 10 <sup>-5</sup>	6.711
0 K	3	Fischer et al. (2014)	6.661	7.417	217.0	4.39	4.788 x 10 <sup>-5</sup>	7.440
300 K	8.7	Hirao et al. (2004)	6.710	7.414	198.0	4.7	4.826 x 10 <sup>-5</sup>	7.186
300 K	8	Lin et al. (2003)	6.882	7.620	141.0	5.7	4.949 x 10 <sup>-5</sup>	6.668

Table E1b – Birch–Murnaghan parameters, initial thermal expansion coefficients and calculated ideal volumes at 323 GPa for literature equations of state shown in Figure 4 with both original and thermally expanded reference volumes.

The third-order Birch Murnaghan EOS is given as

$$P = \frac{3B_0}{2} \left[ \left( \frac{V_0}{V} \right)^{\frac{7}{3}} - \left( \frac{V_0}{V} \right)^{\frac{5}{3}} \right] \left\{ 1 + \frac{3}{4} (B'_0 - 4) \left[ \left( \frac{V_0}{V} \right)^{\frac{2}{3}} - 1 \right] \right\}. \quad (E1)$$

where  $P$  is the system pressure,  $B_0$  is the bulk modulus,  $V_0$  is the reference volume  $V$  is the system volume and  $B'_0$  is the derivative of  $B_0$  with respect to pressure. The values of  $B_0$ ,  $V_0$  and  $B'_0$  for the 3 different temperatures of our Fe-2.7 wt% Si are determined by fitting them as free parameters to the pressure-volume data. These pressure-volume data points were measured by running simulations at each temperature and increasing or decreasing the volume by 1% (when using units of  $\text{\AA}^3/\text{atom}$ ) to either increase or decrease the simulation pressure and give 5 data points that Equation E1 was fitted with to produce an EOS curve. As seen in Figure 4, these equations of state give ideal volumes for the simulations that should give our goal pressure of 323 GPa, so we use these for the 50 simulations at each of the three temperatures. The points that we record should be close enough in value to 323 GPa such that the amount of extrapolation is low and closer to an interpolation of the ideal value. The literature EOS data that we use are all at temperatures significantly lower than the ones that are our undercooled temperatures. Therefore, we extrapolate these equations of state to 3800K such that a comparison can be made with our own EOS, by using an approximated version of thermal expansivity. Each incremental volume change due to an incremental temperature change is defined as

$$V^{new} = V^{old} + V^{old} \left[ \exp \left( \int_{T_i}^{T_f} \alpha(T) dT \right) - 1 \right], \quad (E2)$$

where  $V^{old}$  is the previous  $V^{new}$  volume value and  $\alpha(T)$  is the volumetric expansion coefficient as a function of temperature ( $T$ ), which is integrated between the initial temperature  $T_i$  and the final temperature  $T_f$  for an incremental temperature change of  $T_f - T_i$ . We make an estimate for the  $\alpha$  value at low temperatures by using literature values for Fe-9 wt% Si at 0–8.9 GPa and 300–773 K (Chen et al., 2007). These are given as  $4.74 \times 10^{-5} \text{ K}^{-1}$  for a  $B'_0$  value of 4 and  $4.90 \times 10^{-5} \text{ K}^{-1}$  for a  $B'_0$  value of 5.3, and we use a linear increase between these two values to interpolate the  $\alpha^{init}$  values for the  $B'_0$  values of each literature EOS. We also calculate an  $\alpha^{final}$  value of  $8.727 \times 10^{-6} \text{ K}^{-1}$  at 3800 K, which is equal to  $\frac{1}{V_{4000}} \frac{V_{4000} - V_{3800}}{T_{4000} - T_{3800}}$  using these the known simulation volumes at 3800 K and 4000 K to give 323 GPa. Using these initial and final  $\alpha$  values, we approximate that  $\alpha$  changes linearly from the starting temperature to 3800 K. Equation D2 is evaluated for each  $V^{old}$  to give the  $V^{new}$  values, which are inserted into the Equation as the next  $V^{old}$  values. This is done for increments of 10 K, where the value of  $\alpha$  is calculated as a linear interpolation between the estimated  $\alpha^{init}$  and  $\alpha^{final}$  values, which is then integrated between  $T_i$  and  $T_f$ . This gives a new reference volume of  $V_0^{3800}$  which is used to plot the 3800K thermally expanded points at 323 GPa on the equations of state in Figure 4 using the parameters in Table E1b.

## Section F – Melting Temperature Uncertainty

To calculate the lower bound melting temperature of iron–silicon, we consider the literature estimates. Laser-heated diamond anvil cell experiments have given the melting temperature at 330 GPa as 4000–4200 K for Fe-18 wt%

Si alloy and 4900 K for Fe-33 wt% Si alloy (Lord et al., 2009; Asanuma et al., 2010). Drawing a straight line through these two points, along with the melting temperature for pure iron of 6215 K, and linearly interpolating gives an approximate lower bound value of around 6064 K.

The upper bound value is calculated by using the formula for the depression in the melting temperature due to the presence of silicon, given according to the work of Alfè et al. (2002c) as

$$\chi = \frac{T_m^{Fe}}{S^{ls}} (c_X^s - c_X^l), \quad (F1)$$

where  $T_m^{Fe}$  is the melting temperature of pure Iron, 6215 K,  $S^{ls}$  is the entropy of melting for pure Iron of 0.82, and  $c_X^s$  and  $c_X^l$  are the solid and liquid concentrations of Si respectively (Davies et al., 2019). Alfè et al. (2002a) have determined that there are almost equal concentrations of silicon in the solid and liquid core, so we estimate that  $c_X^s - c_X^l$  equals  $-0.0001$ , representing a very small higher concentration of Si in the liquid than in the solid. This gives a value of  $\chi$  of  $-0.758$  which reduces the melting temperature to an upper bound of around 6214 K and represents the presence of silicon having very little effect on the melting temperature of iron.

## Section G – Waiting Times to Freeze and Uncertainties

Data Point	3800 K Waiting Times (ns)	4000 K Waiting Times (ns)	4200 K Waiting Times (ns)
1	0.02521	0.634178	0.045639
2	0.012555	0.74429	0.057288
3	0.028065	0.321426	0.038502

4	0.023096	0.683724	0.092712
5	0.022792	0.698431	0.058932
6	0.023045	0.872495	0.055205
7	0.02294	0.767156	0.044165
8	0.021401	0.385495	0.087792
9	0.029467	0.426229	0.046929
10	0.024519	0.025037	0.040952
11	0.024803	0.317958	0.051463
12	0.021003	0.041514	0.065572
13	0.035678	0.068589	0.041372
14	0.02212	0.599787	0.04616
15	0.023042	0.075417	0.756243
16	0.020028	0.668165	0.063186
17	0.017238	0.535351	0.041277
18	0.036166	0.319734	0.064948
19	0.010944	0.508593	0.054125
20	0.026794	0.025234	0.052013
21	0.022062	0.492594	0.05636
22	0.018488	0.039658	0.060144
23	0.021734	0.46597	0.054716
24	0.023764	0.036798	0.056295
25	0.020954	0.698777	0.070129
26	0.022426	0.559093	0.068081
27	0.023122	0.238395	0.051624
28	0.0236	0.073551	0.075924

29	0.022419	0.025545	0.064975
30	0.021305	0.2873	0.062289
31	0.013261	0.060165	0.037049
32	0.023219	0.707781	0.034102
33	0.018486	0.020246	0.062154
34	0.019336	0.041466	0.038864
35	0.016788	0.693986	0.062622
36	0.019677	0.889132	0.05169
37	0.033209	0.020487	0.087356
38	0.020471	0.487465	0.025833
39	0.028379	0.511143	0.052223
40	0.034089	0.043427	0.06674
41	0.024453	0.0268	0.073423
42	0.018503	0.297526	0.044497
43	0.024637	0.477772	0.075667
44	0.017936	0.026089	0.070063
45	0.018259	0.431973	0.041676
46	0.015018	0.631391	0.087599
47	0.018995	0.447676	0.037004
48	0.017756	0.692409	0.068653
49	0.025725	0.581912	0.043083
50	0.027982	0.023181	0.062093

*Table G1 – Raw waiting time data collected for 3 different temperatures*

To analyse uncertainty in the critical undercooling value and in the fitted parameters, we must first look at the uncertainty in the data that CNT is fit to.

The uncertainty in the melting temperature, as we have discussed earlier in section 2.2, is very high and thereby creates uncertainty in horizontal uncertainty in the waiting time against undercooling data points. Furthermore, the melting temperature is a parameter used in Equation 1 to fit to the data, so it contributes to the uncertainty in the critical undercooling value. There is vertical uncertainty in the waiting times given by the simple error bars of  $\sigma_0 =$

$\tau_0 / \sqrt{N_{frozen}}$ . However, there is a large additional uncertainty that comes from the uncertainty in the distribution of waiting times. This comes from the misfit of the fitted exponential, given by  $\frac{1}{\tau_0 \exp[-\frac{\tau_x}{\tau_0}]}$  and shown as the red curves in Figure

7, to the actual histograms of waiting times. This is quantified by calculating a derived expected average waiting time of the exponential distribution to compare to the actual average waiting times. There are several more complex ways to integrate the area under the curve to calculate the predicted average value, such as an analytical expression of the mean value of the exponential with use of a prefactor. However, we take a simple numerical approximation to evaluate the mean, which is given as

$$\tau_p = \frac{\sum_{i=1,100} (\tau_i * N_i)}{\sum_{i=1,100} (N_i)}, \quad (E1)$$

where  $\tau_i$  is the lower limit of each bin width and  $N_i$  is each corresponding histogram count.

These estimated predicted waiting times are converted from ns to s and then multiplied by simulation cell volumes  $V$  to give units of  $\text{sm}^3$  ( $\tau_q = \tau_p \times V$ ).

The difference between the observed,  $\tau_v$ , and predicted waiting times,  $\tau_p$ , is what is used to quantify the vertical uncertainty the waiting times points, which is added to the values from  $\sigma_0 = \tau_0 / \sqrt{N_{frozen}}$ , to give the final vertical

uncertainty. The vertical and horizontal uncertainties in the waiting time points are can be seen as the blue error bars in Figure 6b and are what cause the uncertainty in the critical undercooling values along with the uncertainty in the melting temperature parameter,  $T_m$ . We refit Equation 1 to all extremity values of the horizontal and vertical error bars, and from that we find the maximum change in the critical undercooling,  $I_0$  and  $\gamma$  that defines the uncertainties of these values.

Temperature	Calculated Waiting Time (sm <sup>3</sup> )	Predicted Waiting Time (sm <sup>3</sup> )
3800 K	1.54918E-36	1.09682E-36
4000 K	2.58178E-35	2.34646E-36
4200 K	4.89213E-36	2.38724E-36

Table G2 – Calculated waiting times and predicted waiting times from exponential fit

## Section H – Earth Centre Undercooling

Parameter	Value	Reference:
Melting temperature of Fe at Earth's center, $T_m^{cen}$	6500 ± 500 K	Anzellini et al. (2013)
Melting point depression, $\chi_0$	500 – 1000 K	Hirose et al. (2013)
Specific heat capacity, $c_p$	860 ± 86 Jkg <sup>-1</sup> K <sup>-1</sup>	F.D. Stacey (1993)
Thermal expansion coefficient, $\alpha_0$	1.02 – 1.95 × 10 <sup>-5</sup> K <sup>-1</sup>	Gubbins et al. (2003)



Density at Earth's center, $\rho_0$	$12500 \pm 500 \text{ kg m}^{-3}$	Dziewonski & Anderson (1981)
Gruneisen parameter, $\gamma_g$	$1.5 \pm 0.2$	Alfè et al. (2002d)
Gravitational constant, $G$	$6.6743 \times 10^{-11} \text{ N m}^2 \text{ kg}^{-2}$	
Inner core radius, $R_{ic}$	$1.221 \times 10^6 \text{ m}$	

*Table H1 – Parameters used in theoretical calculation of available inner core undercooling for the observed inner core radius, with uncertainties*

The length scale,  $l_p$  is used to define the undercooling at Earth's centre for a given saturation surface radius, and is given as

$$l_p = \sqrt{\frac{3c_p}{2\pi\alpha_0\rho_0 G}}, \quad (\text{H1})$$

where  $c_p$  is specific heat capacity,  $\alpha_0$  is the thermal expansivity coefficient,  $\rho_0$  is the core centre density and  $G$  is the gravitational constant. The undercooling at Earth's centre is defined as

$$\Delta T_0 = T_m^{cen} \left[ 1 - \frac{\exp\left(-2\left(1 - \frac{1}{3\gamma_g}\right)\frac{r^2}{l_p^2}\right)}{\exp\left(-\frac{r^2}{l_p^2}\right)} \right] + \chi_0 \left[ \frac{1}{\exp\left(-\frac{r^2}{l_p^2}\right)} - 1 \right], \quad (\text{H2})$$

where  $T_m^{cen}$  is the melting temperature of pure iron at Earth's centre,  $\gamma_g$  is the Gruneisen parameter,  $r$  is the radius of the undercooled layer, and  $\chi_0$  is the depression of the pure iron melting curve due to light elements, which we assume to be independent of pressure (Hirose et al., 2013).